Paleoceanography and Paleoclimatology

RESEARCH ARTICLE
10.1029/2019PA003806

Key Points:
- High-resolution C and O isotope and XRF data allowed detailed identification of the MECO at Site 702, and suggest a duration of ~300 kyr
- Benthic phytodetritus taxa proliferation and a positive C isotopic excursion predate the start of MECO, suggesting changes in food supply
- Increasing warm-water calcareous nannoplankton taxa during the MECO indicates migration toward higher latitudes due to rising temperature

Supporting Information:
- Supporting Information S1
- Table S1
- Table S2
- Table S3

Correspondence to:
L. Rivero-Cuesta,
lrivero@unizar.es

Citation:
Rivero-Cuesta, L., Westerhold, T., Agnini, C., Dallanave, E., Wilkens, R. H., & Alegret, L. (2019). Paleoenvironmental changes at ODP Site 702 (South Atlantic): Anatomy of the Middle Eocene Climatic Optimum. *Paleoceanography and Paleoclimatology*, *34*, 2047–2066. https://doi.org/10.1029/2019PA003806

Received 12 NOV 2019
Accepted 14 NOV 2019
Accepted article online 27 NOV 2019
Published online 14 DEC 2019

Paleoenvironmental Changes at ODP Site 702 (South Atlantic): Anatomy of the Middle Eocene Climatic Optimum

L. Rivero-Cuesta[1], T. Westerhold[2], C. Agnini[3], E. Dallanave[4], R. H. Wilkens[5], and L. Alegret[1]

[1]Departamento de Ciencias de la Tierra & Instituto Universitario de Ciencias Ambientales, Universidad de Zaragoza, Zaragoza, Spain, [2]MARUM-Center for Marine Environmental Sciences, University of Bremen, Bremen, Germany, [3]Dipartamento di Geoscienze, Università di Padova, Padua, Italy, [4]Faculty of Geosciences, University of Bremen, Bremen, Germany, [5]Hawaii Institute of Geophysics & Planetology, University of Hawai'i at Mānoa, Honolulu, HI, USA

Abstract The Middle Eocene Climatic Optimum (MECO) was an unusual global warming event that interrupted the long-term Eocene cooling trend ca. 40 Ma. Here we present new high-resolution bulk and benthic isotope records from South Atlantic ODP Site 702 to characterize the MECO at a high latitude setting. The MECO event, including early and peak warming as well as recovery to background levels, had an estimated ~300 Kyr duration (~40.51 to ~40.21 Ma). Cross-plots ($\delta^{18}O$ vs. $\delta^{13}C$) suggest that the mechanisms driving coupled changes in O and C isotope values across the MECO were weaker or absent before the event. The paleoecological response has been evaluated by quantitative analysis of calcareous nannofossils and benthic foraminifera assemblages. We document a shift in the biogeographical distribution of warm and temperate calcareous nannoplankton taxa, which migrated toward higher latitudes due to increased temperatures during the MECO. Conversely, changes in the organic matter flux to the seafloor appear to have controlled benthic foraminifera dynamics at Site 702. Benthic phytodetritus exploiting taxa increased in abundance coinciding with a positive $\delta^{13}C$ excursion, ~150 Kyr before the start of the $\delta^{18}O$ negative excursion that marks the start of MECO warming. Our data suggest that paleoecological disturbance in the deep sea predates MECO $\delta^{18}O$ excursion and that it was driven by changes in the type and/or amount of organic matter reaching the seafloor rather than by increased temperature.

1. Introduction

The Eocene was a period of significant change in Earth's climate. It comprises a long-term transition from the greenhouse state of the early Eocene to the icehouse state at the Eocene-Oligocene transition (Miller et al., 1987; Zachos, 2001). The middle to late Eocene cooling was punctuated by short-lived, transient warming events (Edgar et al., 2007; Ivany et al., 2008; Sexton et al., 2006; Tripati, 2005; Wade & Kroon, 2002), with the Middle Eocene Climatic Optimum (MECO; Bohaty & Zachos, 2003) being one of the most puzzling events described. The MECO was first recognized by a negative oxygen isotopic excursion (OIE; approximately –1‰ in $\delta^{18}O_{bulk}$ and $\delta^{18}O_{benthic}$ records) at different Southern Ocean sites (Bohaty & Zachos, 2003). It was further documented at globally distributed ocean drilling sites and on-land sections (Bohaty et al., 2009; Boscolo Galazzo et al., 2014; Jovane et al., 2007; Spofforth et al., 2010), hence considered a global event. The OIE recorded across the MECO has been interpreted mainly as a temperature signal as ice sheets were likely small or absent during the Eocene (Bohaty & Zachos, 2003; Edgar et al., 2007), suggesting a transient global warming of 4–6 °C in both surface and deep waters (Bohaty & Zachos, 2003; Bohaty et al., 2009; Bijl et al., 2010).

The MECO OIE peak appears to be synchronous with the base of Chron C18n.2n (40.14 Ma, Gradstein et al., 2012), providing a reliable age constraint (Bohaty et al., 2009). Another useful dating event is the short planktonic foraminifera biozone E12 (Berggren & Pearson, 2005), defined by the total range of *Orbulinoides beckmanni*, that was believed to coincide with the MECO event (e.g., Bohaty et al., 2009) However, this species is diachronous, as it appeared earlier at low latitudes and successively spread toward higher latitudes (Edgar et al., 2010). Nannofossil biozones provide further tie points across the MECO (Agnini et al., 2014) even at high latitudes (Villa et al., 2008; Wei & Thierstein, 1991), although there is also slight diachroneity of certain biostratigraphic events between high and low latitudes

(Bohaty et al., 2009). In order to compare and correlate the MECO among different sites and in addition to the identification of the base of Chron C18n.2n, high-resolution carbon and oxygen isotope records are arguably the best tool available due to their distinctive patterns (Bohaty et al., 2009). Estimations of MECO duration based on isotopic records vary from ~500 Kyr (Bohaty et al., 2009), ~600 Kyr (Bohaty & Zachos, 2003) to ~750 Kyr (Edgar et al., 2010). Robust age models are needed to better constrain the duration of this event, to discuss its mechanisms, and to assess its relation with orbital cycles (Giorgioni et al., 2019; Westerhold et al., 2014, 2015).

Like other Eocene warming events, the MECO is associated with a decline in carbonate accumulation at abyssal sites (Lyle et al., 2005) and related increase in atmospheric pCO_2 concentrations (Bijl et al., 2010). However, it usually lacks a clear carbon isotope excursion (CIE) accompanying the OIE, with carbon isotopic values even rising rather than declining during MECO warming (Bohaty & Zachos, 2003). Some study sites show records of a brief CIE (−0.5‰ $\delta^{13}C_{bulk}$) coinciding with OIE peak conditions, but this is not consistent across sites (Boscolo Galazzo et al., 2014). The duration of the MECO, its gradual warming/rapid cooling pattern, and its unusual CIE trend have raised questions about how well we understand carbon cycle mechanisms across warm periods, with models struggling to recreate the trends displayed by MECO records (Sluijs et al., 2013). The characteristics of this event provide a unique opportunity to analyze the complex relationship between climate and the carbon cycle during past periods of increased atmospheric pCO_2 and global warming on a hundreds of Kyr timescale.

Carbon-containing organic matter is an important component of the carbon cycle, and its cycling is driven by both abiotic and biotic processes. Oceanic organic matter through the biological pump was the main regulator of atmospheric CO_2 during the Eocene (Hilting et al., 2008). However, only a small part of the organic matter produced in the surface reaches the deep sea, especially at high latitudes (Diester-Haass & Faul, 2019) where recycling across the water column is particularly high. The remaining organic carbon is consumed by deep-sea heterotrophs (e.g., benthic foraminifera) and ultimately removed from the ocean-atmosphere system by burial (Arndt et al., 2013). Paleoecological studies across the MECO have reported shifts in both surface and deep-sea faunas (e.g., Toffanin et al., 2011; Boscolo Galazzo et al., 2014; 2015), suggesting changes in the biological pump. Surface primary productivity has been reported to increase or decrease depending on the study site (e.g., Luciani et al., 2010; Takata et al., 2013; Toffanin et al., 2011, 2013). Similarly, reported changes in benthic foraminifera assemblages across the MECO range from significant and transient restructuring of the fauna (Ocean Drilling Program [ODP] Site 738, Moebius et al., 2014) to unchanged benthic assemblages (ODP Site 1263, Boscolo Galazzo et al., 2015). In order to characterize this perturbation of the global carbon cycle and to improve our understanding of its paleoenvironmental consequences, we generated geochemical and paleontological proxies across the MECO interval at ODP Site 702 (Leg 114, South Atlantic Ocean). New, high-resolution bulk and benthic $\delta^{18}O$ and $\delta^{13}C$ isotope records as well as XRF, magnetostratigraphy, and calcium carbonate content (%$CaCO_3$) are presented to assess paleoceanographic changes. Paleoecological inferences are based on calcareous nannofossil and benthic foraminifera assemblages.

A comprehensive reconstruction of the paleoceanographic conditions of surface and deep-sea realms at this high latitude site is here presented, addressing the changes in organic carbon flux across the MECO and its consequences on deep-sea biota. Additionally, we provide constrains on the timing of the $\delta^{18}O$ and $\delta^{13}C$ isotopic excursions in the bulk and benthic records identifying their similarities and differences, which may contribute to improve our understanding of the mechanisms triggering and controlling the MECO.

2. Location and Setting

ODP Site 702 was drilled during Leg 114 (March–May 1987) in the central area of the Islas Orcadas Rise (50° 56.760′S, 26°22.122′W, 3,083.4 m water depth) in the South Atlantic Ocean (Figure 1). Islas Orcadas is a north-northwest-trending aseismic ridge more than 500 km long, 90 to 180 km wide, and over 1,000 m above the adjacent seafloor (Ciesielski & Kristoffersen, 1988). Circumpolar Deep Water bathes the central region of the Islas Orcadas Rise, and surface waters have a strong easterly flow created by the Antarctic Circumpolar Current (Reid et al., 1977). The Antarctic Convergence Zone, or polar front, today lies 60 km north of Site 702 (Gordon et al., 1977).

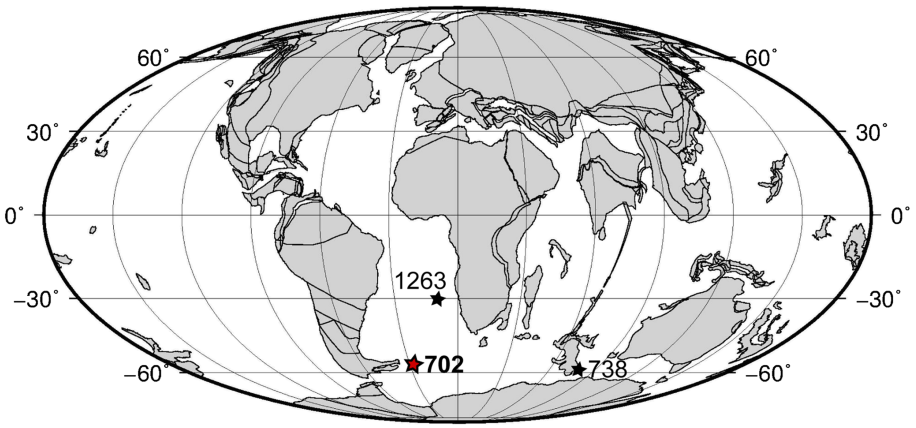

Figure 1. Map of ODP sites where benthic foraminifera assemblages have been studied across the MECO: Site 702 (this study), Site 738 (Moebius et al., 2014), and Site 1263 (Boscolo Galazzo et al., 2015). High-resolution isotope and XRF data from these sites have been used to generate the age model used in this study. Approximate positions at 40 Ma are plotted on a paleogeographic reconstruction from the Ocean Drilling Stratigraphic Network (GEOMAR, Kiel, Germany).

The Islas Orcadas Rise was likely formed during the early Paleogene, at a propagating rift that also produced the Meteor Rise (Ciesielski & Kristoffersen, 1988). Rifting and seafloor spreading separated the Islas Orcadas and Meteor rises in the Eocene, forming a deep passageway that allowed less-restricted communication of deep water from the South Atlantic to the north (Ciesielski & Kristoffersen, 1988). Site 702 subsided to near its present water depth after the late Eocene, suggesting that late Paleocene to Eocene subsidence of Site 702 was only minor; by middle to late Eocene, the polar front was located south of the Islas Orcadas Rise (Ciesielski & Kristoffersen, 1991). Extensive deposition of homogeneous nannofossil ooze and chalk, with relatively minor contribution of foraminifera (<10%) and a high carbonate content (85% to 95%; Ciesielski & Kristoffersen, 1991), took place at lower bathyal (1,000–2,000 m) paleodepths at that time (Ciesielski & Kristoffersen, 1991).

The occurrence of abundant, diverse, and well-preserved benthic foraminifera and calcareous nannofossils across middle-late Eocene sediments, together with its relatively expanded and continuous record, make Site 702 a suitable location to perform paleontological and geochemical analyses at high resolution.

3. Materials and Methods

ODP Site 702 Hole B was sampled at the International Ocean Discovery Program Bremen Core Repository. Sediment samples between Core 8X, Section 1, interval 44–46 cm (63.74 m below sea floor [mbsf]) and Core 10X, Section 1, interval 98–100 cm (83.28 mbsf) were taken at high resolution (see details below). The MECO was first identified at Hole 702B by a sharp OIE between 75 and 70.5 mbsf (Bohaty et al., 2009), which served as a baseline for our study.

3.1. Inorganic Geochemistry and XRF Measurements

Bulk stable C and O isotope analyses were performed on 238 sediment samples between 81.00 and 64.90 mbsf (5 to 10 cm resolution, ~4–8 Kyr; supporting information Table S1). Analyses were performed at the MARUM Isotope Laboratory (Bremen University) using a Finnigan MAT 252 gas isotope ratio mass spectrometer with Kiel III/Kiel IV automated carbonate preparation device. Data are reported relative to the Vienna Pee Dee Belemnite international standard, determined via adjustment to calibrated in-house standard (Solnhofen limestone) and NBS-19. The standard deviation of house standard over the measurement period was 0.04‰ for $\delta^{13}C$ and 0.07‰ for $\delta^{18}O$. Species-specific C and O isotope analyses were carried out on benthic foraminiferal tests, using a set of 72 samples between 80.85 and 64.90 mbsf, with a sample resolution between 50 and 8 cm (higher around the OIE). Between 8 and 15 specimens of well-preserved *Nuttallides truempyi* were analyzed per sample. Large specimens from the ≥100 μm fraction were used to avoid intraspecific variation of juvenile and adult specimens. Bulk wt%$CaCO_3$ was analyzed on 41 samples between 80.85 and 64.90 mbsf (sampling resolution from 1.5 m to 25 cm, with higher resolution across the OIE).

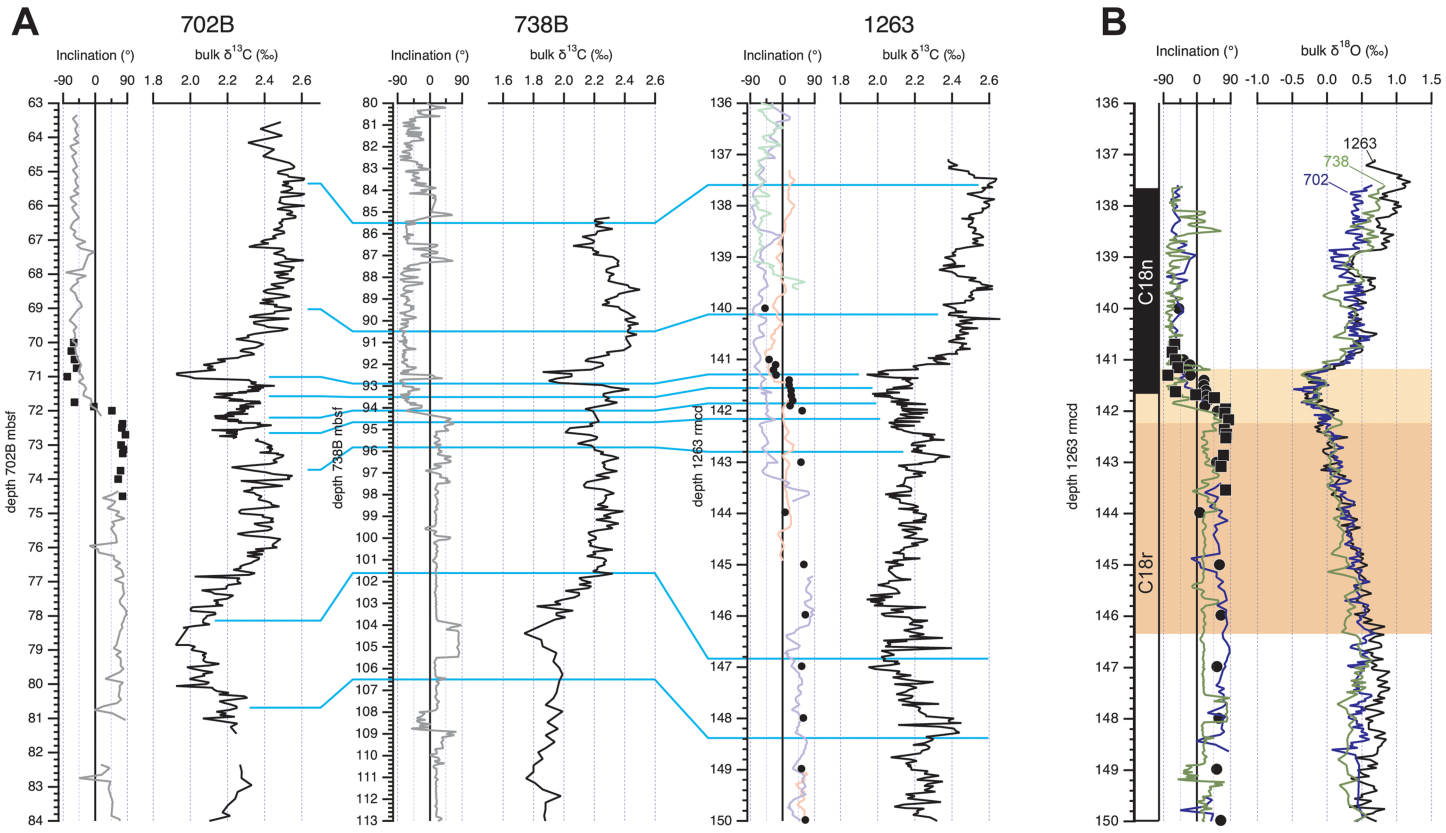

Figure 2. (a) Correlation of Hole 702B with Hole 738B and Site 1263 by high-resolution carbon isotope records (bulk sediment) and (b) magnetostratigraphic data. Data in Table S5.

The analyses were performed with a manocalcimeter (Geoservices) by addition of 5 ml of HCl (50 %) to 1 g of pulverized sediment. The pCO_2 produced during this reaction was measured in vacuum, and the result is given in % $CaCO_3$ of the total sediment analyzed.

Sediment Cores 702B7X to 702B10X from Hole 702B (archive half) were analyzed with an XRF Core Scanner III at MARUM-University of Bremen. Data were obtained every 2 cm down core over a 1 cm^2 area using a generator setting of 10 kV, 0.150 mA, and a sampling time of 15 s. XRF Scanner III was operated with a Canberra X-PIPS Silicon Drift Detector (Model SXD 15C-150-500) with 150 eV X-ray resolution, the Canberra Digital Spectrum Analyzer DAS 1000 and an Oxford Instruments 100W Neptune X-ray tube with rhodium (Rh) target material. Data are complementary to the set published in Westerhold et al. (2018).

3.2. Magnetostratigraphy

Shipboard paleomagnetic measurements of the natural remanent magnetization (NRM) were performed on the archive halves after maximum alternating field (AF) cleaning of 5 or 9 mT (Clement & Hailwood, 1991). Despite the low level of demagnetization, this analysis resulted in a shift from negative (up-pointing) to positive (down-pointing) paleomagnetic inclination interpreted as the C18n.2n-C19r Chron boundary. However, the shipboard data do not provide a continuous and fully reliable magnetic polarity record through the interval of interest at Hole 702B, and the archive halves measurements are not supported by discrete sample analysis because the intensity of the NRM signal is too low for the equipment available at the time. The CIE related to the MECO has been found near the C18n.2n-C18r Chron boundary (Bohaty et al., 2009). In order to improve the shipboard-based magnetostratigraphy, we collected a total of 23 oriented discrete samples between 70.14 and 74.43 mbsf (Figure 2), where this Chron boundary was originally placed (Clement & Hailwood, 1991). After selecting sedimentary layers not affected by coring deformation, samples were collected by pushing standard 8 cm^3 plastic cubes into the core.

To determine the paleomagnetic component of the NRM, all samples were demagnetized using three-axes AF technique, adopting 5 mT steps from 5 to 50 mT and 10 mT steps from 50 up to 100 mT, measuring the NRM after each demagnetization step. After AF demagnetization, we investigated the magnetic mineralogy of the samples by means of isothermal remanent magnetization (IRM) acquisition on a representative set of eight samples. Samples were magnetized using 22 steps with field ranging from 10 to 700 mT, and the IRM was measured after each step. All magnetic remanence measurements were performed with a 2G-Enterprises cryogenic magnetometer placed in line with an ASC AF demagnetizer and a pulse magnetizer (Mullender et al., 2016) at the University of Bremen.

The characteristic remanent magnetization (ChRM) of the sediment has been isolated by means of visual inspection of vector end points demagnetization diagrams (Zijderveld, 1967). We isolated the vector components linearly decaying to the origin of the demagnetization axes using the principal component analysis of Kirschvink (1980). ChRM components failing to trend linearly to the origin of the axes are estimated applying the spherical statistic of Fisher (1953) to the vector end points. Since the cores are azimuthally not oriented, the magnetic polarity stratigraphy has been interpreted using only the inclination of the ChRM, whereby directions with negative inclination were acquired during a normal geomagnetic field, while positive inclination represents reversed field. Analyses were performed using the PuffinPlot freeware (Lurcock & Wilson, 2012).

3.3. Correlation and Age Model

Records of carbon and oxygen stable isotopes on bulk carbonate and benthic foraminifera are key to identifying and correlating the MECO between different ocean regions (Bohaty & Zachos, 2003; Bohaty et al., 2009). Our new, high-resolution bulk carbon isotope records were used to correlate ODP Sites 702B, 738B, and 1263 based on the identification of characteristic and unique features across magnetic polarity Chrons C18r and C18n2n (Figure 2). Bulk oxygen isotope and magnetostratigraphic data (inclination) reinforce the correlation confirming that the reversal from C18r to C18n2n is located in the second of three prominent carbon isotope swings in the peak-MECO. After depth correlation, the age model for ODP Site 1263 has been adopted providing a consistent stratigraphic framework for the sites across the MECO interval. The age model for Site 1263 is based on astronomical tuning of high-resolution bulk carbonate stable carbon isotope data to the La2010b (Laskar et al., 2011) solution for orbital eccentricity. Variations in Site 1263 bulk carbon isotope data show clear imprint of short (100 Kyr) and long (405 Kyr) eccentricity, as already documented and applied for orbital tuning for the early and middle Eocene records from Site 1263 (Westerhold et al., 2015, 2017, 2018). Tuning was done by correlating the long eccentricity cycle related lighter carbon isotope data to the maxima in the La2010b eccentricity solution (Figure S1). Bulk carbon isotope data from Hole 702B reinforce the tuning of Site 1263 carbon isotope data, particularly in 405 Kyr eccentricity cycle 102 where Hole 702B data show a clearer expression of the cycle compared to Site 1263 as already presented in Westerhold et al., 2018 (see Figure S6 and S7 therein). This procedure results in a new astronomically tuned age model fully encompassing the MECO event. A previous tuned age model combining International Ocean Discovery Program Expedition 320 records from the equatorial Pacific with records from ODP 1051, 1172A, and 1260 (Westerhold et al., 2014) is lacking of high-quality, high-resolution stable isotope data due to dissolution of carbonate during the MECO and rely on low quality magnetostratigraphic data from 1172A.

3.4. Benthic Foraminifera

Quantitative analyses on benthic foraminifera were carried out on 36 samples between 83.29 and 63.75 mbsf; sampling resolution varied from 1.5 m to 25 cm, ~120 to 20 Kyr (higher resolution across the OIE). Samples were oven-dried (<50 °C for 24 hr), weighed, and disaggregated in $(NaPO_3)_6$ for 3 hr. Each sample was sieved under running water, and the ≥63 μm size fraction was collected, oven-dried (<50 °C for 24 hr), and weighed again.

Assemblage work was performed on representative splits of around 300 specimens per sample. A total of 73 taxa (70 calcitic and 3 agglutinated) was recognized at species or higher taxonomic level (Table S2). Classification at the generic level mainly follows Loeblich and Tappan (1987), except for uniserial taxa (Hayward et al., 2012). Species identification follows Tjalsma and Lohmann (1983), Van Morkhoven et al. (1986), Müller-Merz and Oberhänsli (1991), Ortiz and Thomas (2006), Holbourn et al. (2013), Boscolo

Galazzo et al. (2015), and Arreguín-Rodríguez et al. (2018). Preservation of foraminiferal tests is commonly good, suitable to detect diagnostic morphological features. The most representative specimens were photographed using the SEM imaging facilities at the University of Zaragoza (Spain) (Figure S2).

The relative abundance of each species was calculated from the raw data matrix. Diversity (Fisher-α) and dominance indices (Murray, 1991) and the percentage of calcareous and agglutinated tests were calculated. Taxa were assigned to infaunal or epifaunal morphogroups according to their morphology, following Jones and Charnock (1985), Corliss and Chen (1988), and Corliss (1991). The TROX model (Jorissen et al., 1995) was followed to infer food supply and oxygenation at the seafloor according to the microhabitat distribution of benthic foraminifera, which is extrapolated by comparing with modern, morphologically similar taxa (e.g., Jorissen, 1999). Note that foraminifera are not static but actively move through the sediment (e.g., Bornmalm, 1997; Fontanier et al., 2002; Gooday & Rathburn, 1999; Gross, 2000; Jorissen, 1999), and this may lead to inaccuracies when assigning microhabitats.

Hierarchical cluster analysis was performed (PAST package, Hammer et al., 2001) on a data matrix containing all common taxa (species >1.5% in at least one sample) using the Pearson similarity index and the unweighted pair-group (UPGMA) algorithm. Detrended Correspondence Analysis (DCA) was carried out to further analyze the results derived from clustering and to investigate the relationship between foraminifera and environmental variables (Hammer & Harper, 2005). For further paleoenvironmental assessment, the longitudinal axis of the species *Bulimina elongata* was measured (15 to 57 measures per sample) using an Olympus SC50 camera and Stream Basic software.

3.5. Calcareous Nannofossils

A total of 46 samples was analyzed between 81.18 and 65.20 mbsf with a variable sample resolution that increases up to 10–20 cm from 74.50 to 70.50 mbsf and results in a time resolution of 8 and 33 Kyr, respectively. Standard smear slides were processed following the routine method described in Bown and Young (1998). Preliminary qualitative estimate of the abundance and preservation state of calcareous nannofossil assemblages was performed for all samples. Samples were examined under a Zeiss light microscope at 1,250X magnification. The taxonomy adopted is that of Perch-Nielsen (1985) and Agnini et al. (2014). The adopted biostratigraphic schemes are those of Martini (1971), Okada and Bukry (1980), and Agnini et al. (2014). Counts on selected taxa were performed on a given area (1 mm^2; Backman & Shackleton, 1983) for biostratigraphical and paleoecological aims. The number of specimens on a fixed area in a truly pelagic depositional setting provides an estimation of the productivity of the taxa examined even if the variable amount of sediment could bias the absolute number, but previous studies have shown that the standard deviation on different replicas is always <2–5% (Agnini et al., 2016). Biohorizon nomenclature follows that given by Agnini et al. (2014): base (B), base common (Bc), top (T), and top common (Tc).

3.6. Accummulation Rates

Linear sedimentation rate and dry bulk density data from the shipboard report (Ciesielski & Kristoffersen, 1988) were extrapolated to calculate benthic foraminiferal (BFAR; Herguera & Berger, 1991) and coarse fraction (CFAR) accumulation rates (ARs). BFAR values are considered as a proxy for total organic matter flux reaching the seafloor (Gooday, 2003; Jorissen et al., 2007), and CFAR values are an approximation of planktonic foraminiferal ARs (Diester-Haass, 1995).

ARs were also calculated according to the sedimentation rates calculated with the age model derived from correlation with Site 1263, although the trends are very similar to the ARs calculated with the linear sedimentation rate from shipboard data.

4. Results

4.1. Stable Isotope Trends

Results from stable O and C isotope analyses performed on bulk carbonate follow the trends observed by Bohaty et al. (2009) but now resolve Hole 702B record at much higher resolution (every 5 to 10 cm), revealing cyclic variations throughout (Figure S3).

Oxygen isotope values of bulk sediment ($\delta^{18}O_{bulk}$) vary between 0.65‰ and −0.34‰ (maximum amplitude 0.99‰; Figure 3). The lowermost part of the section (from 81.00 to 75.20 mbsf) shows consistently high

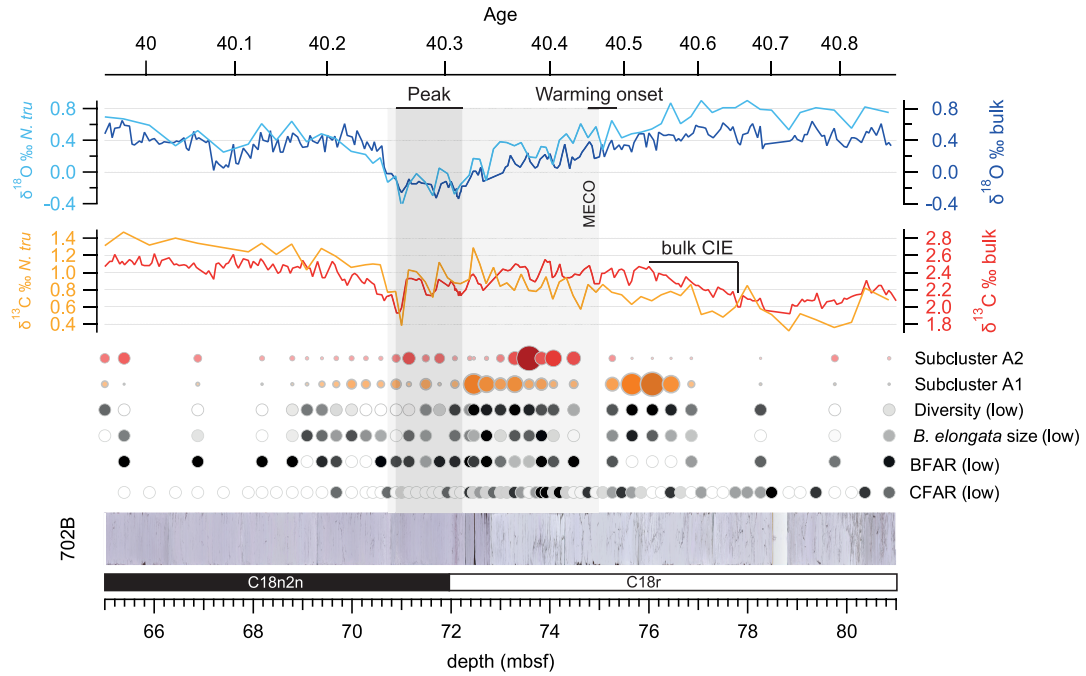

Figure 3. Bulk (darker lines) and benthic (*Nuttallides truempyi*, lighter lines) isotopic data from Site 702 plotted against depth (mbsf). Visual representation of relative abundances of benthic Subclusters A1 (red dots) and A2 (orange dots), benthic foraminifera diversity (Fisher-α), *B. elongata* maximum test size, benthic foraminifera accumulation rates (BFARs) and coarse fraction accumulation rates (CFARs) (darker dots represent lower values). Age derived from this study.

values (>0.20‰). A gradual decreasing trend is recorded between 75 and 72.15 mbsf, where the minimum $\delta^{18}O_{bulk}$ value is recorded. Negative $\delta^{18}O_{bulk}$ values are concentrated within 73.05 and 70.60 mbsf and shows three distinct negative peaks at 72.15, 71.70, and 71.00 mbsf (MECO OIE peak conditions), and this pattern is also present in the other O and C isotopic records. The last peak is followed by a very rapid +0.59‰ increase in $\delta^{18}O_{bulk}$ within a 0.4 m interval (between 71.00 and 70.60 mbsf). $\delta^{18}O_{bulk}$ recover to preexcursion values toward the top of the studied interval, interrupted by a short-term decrease to ~0‰ $\delta^{18}O_{bulk}$ between 67.70 and 67.20 mbsf.

Overall, oxygen isotope values measured on *N. truempyi* ($\delta^{18}O_{benthic}$) parallel the trend observed in $\delta^{18}O_{bulk}$ (Figure 3), showing a slightly larger variability from 0.90‰ in the lower part of the studied interval to −0.44 ‰ (maximum amplitude 1.35‰) in the middle part. While the negative excursion of the $\delta^{18}O_{benthic}$ record starting at 74.50 mbsf has a similar excursion rate (−0.56‰ across ~3 m) than the $\delta^{18}O_{bulk}$ record, the second part of the excursion (72.86 to 71.00 mbsf) shows a higher excursion rate in the $\delta^{18}O_{benthic}$ record: a −0.74‰ drop within a 1.86 m interval. The three negative peaks observed in $\delta^{18}O_{bulk}$ are also recorded in $\delta^{18}O_{benthic}$, which display minimum values at the third peak (71 mbsf). Similar to the $\delta^{18}O_{bulk}$ trend, the recovery in $\delta^{18}O_{benthic}$ values is recorded within a short interval (+0.87‰ increase between 71 and 69.67 mbsf), but the length of the recovery interval is twice as long in $\delta^{18}O_{benthic}$ compared to $\delta^{18}O_{bulk}$ (~0.40 m). Post-excursion $\delta^{18}O_{benthic}$ values are lower than preexcursion values by −0.2‰.

Carbon isotope values of bulk sediment ($\delta^{13}C_{bulk}$) range between 2.62‰ and 1.92‰ (maximum amplitude 0.69‰; Figure 3). A gradual increasing trend in $\delta^{13}C_{bulk}$ is observed from the lower to the middle part of the studied interval, between 78.35 (1.96‰) and 76.00 mbsf (2.47‰), followed by an interval of relatively constant high $\delta^{13}C_{bulk}$ values ranging between 2.25‰ and 2.47‰. A decreasing trend in $\delta^{13}C_{bulk}$ values starts ~73.00 mbsf, and three minor, negative peaks are distinguished at 72.20, 71.60, and 70.95 mbsf, the last one being more significant. They coincide with the three negative excursions in $\delta^{18}O_{bulk}$ and $\delta^{18}O_{benthic}$ values. Recovery to preexcursion values is recorded within a 1.2 m thick interval (between 70.90 and 69.70 mbsf), and $\delta^{13}C_{bulk}$ values remain relatively constant (>2.32‰) above the recovery interval. A few, below-average $\delta^{13}C_{bulk}$ values are recorded in coincidence with relatively low $\delta^{18}O_{bulk}$ values at ~67.20 mbsf.

Benthic carbon isotope values ($\delta^{13}C_{benthic}$) fluctuate between 1.47‰ and 0.32‰, showing a larger variability (max. amplitude 1.14‰) than $\delta^{13}C_{bulk}$ values (Figure 3). Despite minor differences between $\delta^{13}C_{benthic}$ and $\delta^{13}C_{bulk}$ records, they show similar trends, with minimum values in the lower part of the study interval and higher values in the uppermost part. Short-term trends in the $\delta^{13}C_{benthic}$ record are difficult to assess due to the larger variability and lower sampling resolution. However, the gradual increase in $\delta^{13}C_{benthic}$ values is interrupted across interval 72.37–70.57 mbsf, and a three-peaked negative excursion (approximately −0.6‰) can be distinguished. The three negative peaks in $\delta^{13}C_{benthic}$ (at 72.19, 71.48, and 71.00 mbsf) coincide with those identified in $\delta^{13}C_{bulk}$, $\delta^{18}O_{bulk}$, and $\delta^{18}O_{benthic}$ values, with the latter peak recording the most prominent negative excursion.

Cross-plots of $\delta^{18}O$ versus $\delta^{13}C$ values are useful to assess the correlation between these two proxies. A linear regression comprising all samples within the MECO event shows a positive correlation between $\delta^{18}O_{bulk}$ and $\delta^{13}C_{bulk}$ values (Figure S4a). No correlation is observed during the pre-MECO interval, where increasing $\delta^{13}C$ values are recorded while $\delta^{18}O$ values remain high. The MECO linear regression of the $\delta^{18}O_{bemthic}$ versus $\delta^{13}C_{benthic}$ cross-plot (Figure S4b) shows a less pronounced slope. In this case, the number of samples ($n = 72$) could partially account for the poor linear regression fit and different slope result compared to the bulk record ($n = 238$). Benthic MECO regression line is plotted against the regression lines of other Eocene warming events for comparison (Figure S4c).

4.2. Rock Magnetism and Paleomagnetism

The maximum IRM after, magnetization with 0.7 T inducing field, is between 0.3 and 0.4 mA/m. In all samples, 77% to 85% of the maximum IRM is reached within a magnetizing field of 100 mT (Figure S5a), indicating that the magnetic mineralogy is dominated by a low coercivity phase, likely consisting of magnetite. This result supports the reliability of the presented paleomagnetic data set, because the ChRM directions were isolated by AF demagnetization up to a peak field of 100 mT.

The intensity of the NRM ranges around 10^{-5} and 10^{-4} A/m. We obtained ChRM directions suitable for magnetic polarity stratigraphy from 17 samples out of 23 (74%). Of these 17, 11 have been obtained by linear interpolation of vector end points (Kirschvink, 1980). On six specimens, the vector end points are found to decay toward the demagnetization axes origin without a clear linear pattern, and the ChRM directions have been estimated by calculating the Fisher (1953) mean of the vector end points themselves, an approach already successfully used in analyses of paleomagnetic data (Tauxe et al., 2012) (Figure S5c and Table S3). The directional data set is organized in two modes, whereby seven directions have negative inclination while 10 have positive inclination. The sampled stratigraphic interval straddles two cores, namely, 702B-8X and 702B-9X. Due to the lack of declination control (in particular between the two cores), we estimated the average direction of the two modes, and of the whole data set, using the inclination-only approach of McFadden and Reid (1982; Figure S5d).

The inclination data are plotted together with the inclination of the continuous archive halves measurement (Clement, 1991). There is a substantial agreement between the two data sets in the interval from 70 to 72.3 mbsf. Our new discrete-sample based magnetostratigraphy constrains at 71.99 mbsf, the depth of the magnetic polarity reversal that was originally interpreted as the C18n.2n-C18r Chron boundary (Clement & Hailwood, 1991; Figure 2 and S6). Shipboard measurements are characterized by a gap between 72.25 and 74.35 mbsf, limiting the reliability of the position originally proposed for the Chron boundary (Clement & Hailwood, 1991). Our new data clearly show consistent positive ChRM inclination below 71.99 mbsf (i.e., reversed magnetic polarity).

4.3. Benthic Foraminiferal Assemblages

Benthic foraminifera are strongly dominated by calcareous taxa (98% of the assemblages) matching the continuously high (~80%) $CaCO_3$ content recorded. Diversity (Fisher-α index) ranges between 10.8 (minimum at 73.29 mbsf) and 18.2 (maximum at 66.88 mbsf) (Figure 4). Low diversity values (below average Fisher-α 14.3) are mostly recorded between 78.26 and 72.08 mbsf. In contrast, dominance oscillates, showing the highest (above average 0.20) but also the lowest values between 79.76 and 72.46 mbsf.

Assemblages show changes in relative abundance of species across the studied interval. A classical hierarchical cluster analysis of species ($n = 33$) shows two main clusters (A and B) and four subclusters (A1, A2, B1,

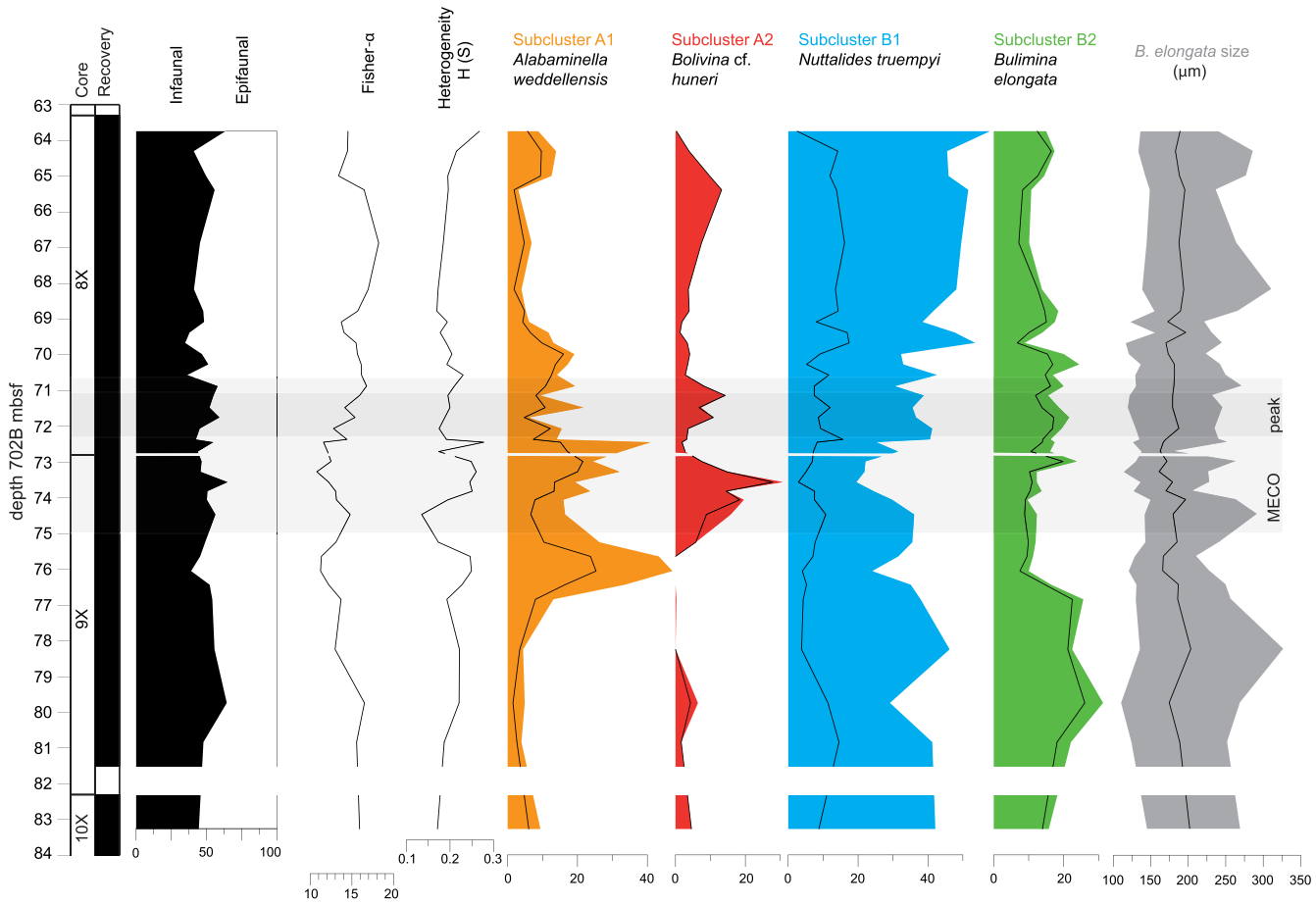

Figure 4. Benthic foraminifera quantitative analysis at Site 702. Morphotypes (infaunal/epifaunal ratio), diversity (Fisher-α index), and dominance indices and relative abundance of Subclusters A1 (orange), A2 (red), B1 (blue), and B2 (green), including their most representative species (black lines within each color plot, species names in the figure). The gray plot represents the range of *Bulimina elongata* test sizes (black line = average).

and B2) with similarity <0 (Figure S7). Cluster B contains more species (n = 24) and has a higher relative abundance (up to 72.8% of the assemblages) than Cluster A.

In Subcluster A1, the main component is *Alabaminella weddellensis*, followed by *Caucasina* sp. and *Epistominella exigua*. These taxa have flattened trochospiral tests and an inferred epifaunal habitat. Infaunal taxa (e.g., *Buliminella grata* and *Buliminella beaumonti*) are a minor component of Subcluster A1 (<2.25%). The relative abundance of this subcluster strongly varies across the studied interval from 3.07% to 47.19%, with the largest changes and highest values recorded between 76.86 and 69.39 mbsf (highest value at 76.07 mbsf) (Figure 4). Subcluster A2 only includes two species, *Bolivina* cf. *huneri* and *Fursenkoina* sp. 2, the former being the main component. Both species are believed to have had an infaunal mode of life, and they show substantial ornamentation on their tests (Figure S2). The relative abundance of Subcluster A2 increases between 74.48 and 70.89 mbsf (maximum at 73.58 mbsf). Both subclusters are scarce in the lower part of the studied interval, and their relative abundances show a negative correlation in the middle and upper part of the investigated section.

Subcluster B1 is the most diverse one, including 19 species. *Nuttallides truempyi* is the most abundant species, followed by *Globocassidulina subglobosa*, *Cibicidoides micrus*, *Oridorsalis umbonatus*, *Bulimina alazanensis*, and *Cibicidoides praemundulus* (each of them >5% in relative abundance). The lowest values of this subcluster (average < 37.26%) are recorded between 76.45 and 72.46 mbsf (Figure 4). Subcluster B2 shows the smallest changes in relative abundance across the study interval, and unlike the other subclusters, it is more abundant in the lower part (between 83.29 and 76.45 mbsf). It is dominated by *Bulimina elongata*, while the other four species forming this subcluster show relative abundances <5%. Due to the different

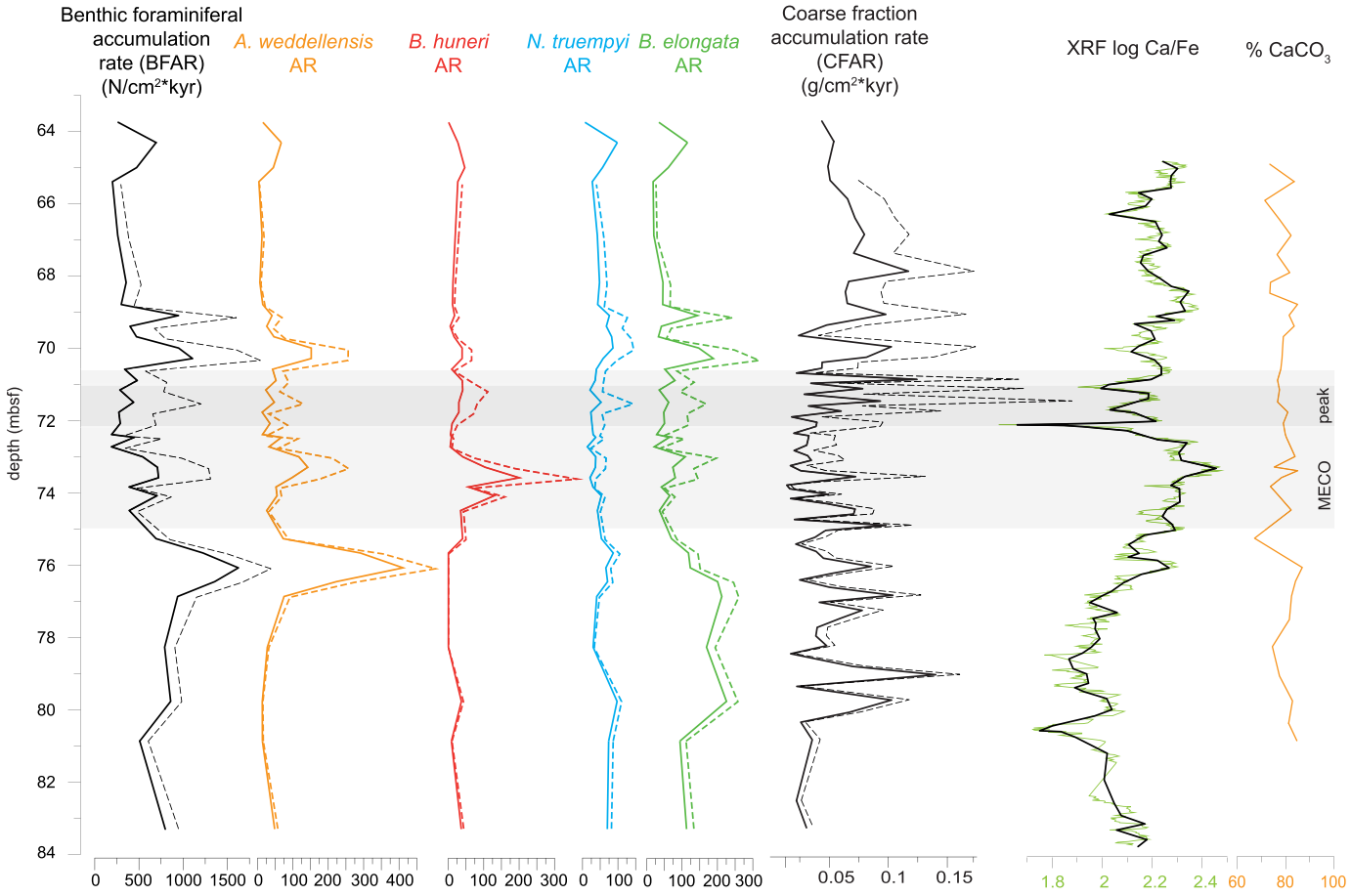

Figure 5. Accumulation rates (ARs), XRF, and $CaCO_3$ %. Solid lines represent ARs calculated with the linear sedimentation rate from shipboard data. Dashed lines are ARs calculated with sedimentation rates derived from Site 702 age model (this study).

abundance trend of *B. elongata* as compared to other species, the length of this taxon was measured across the study interval. Average values (181.91 μm) and minimum values do not show any significant changes (Figure 4), but maximum test sizes have lower values between 76.07 to 68.79 mbsf (lowest at 72.72 mbsf).

In order to better understand and interpret the paleoecological changes related to subcluster abundance fluctuations, a DCA analysis was performed on the same data set as the cluster analysis (with species >1.5% in relative abundance; Figure S8). Species from Cluster A fall within positive values of Axis 1, while Cluster B shows Negative Axis 1 values except for one outlier. Species from Subcluster A2 show high positive values along Axis 2, while Subcluster A1 values are negative along Axis 2. Cluster B shows Intermediate Axis 2 values, ranging between 25 and −40.

4.4. Benthic foraminifera and Coarse Fraction Accumulation Rates

BFARs and species-specific ARs have been calculated for the dominant species of each subcluster. Calculations were made with assumed constant sedimentation rates (Ciesielski & Kristoffersen, 1988) and with sedimentation rates derived from Site 702 age model; however, both calculations show similar overall trends and range of values (Figure 5).

BFARs show average values in the lower part of the study interval, shifting to lower values between 72.72 and 70.58 mbsf and between 68.79 and 65.00 mbsf. *Alabaminella weddellensis* has low ARs values across the section, showing larger values in the intervals 76.75–75.66, 73.58–73, and 70.28–69.99 mbsf. *Nuttallides truempyi* and *B. huneri* ARs are stable except for a noticeable increase of the latter between 74.07 and 73.19 m. In contrast to the other species, *B. elongata* ARs are higher in the lower part of the

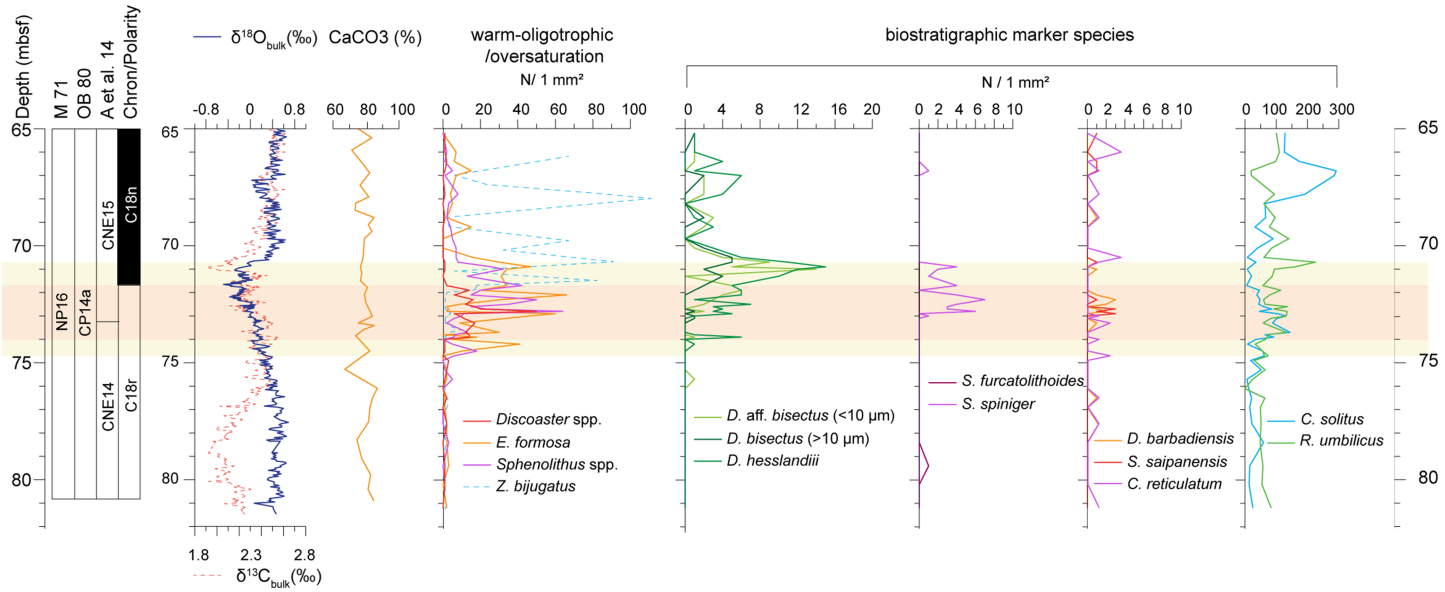

Figure 6. Calcareous nannofossils abundances plotted against depth. Biozones recognized are shown on the left and abundances of relevant biostratigraphic markers on the right. Relative abundance of warm species and the isotopic records are plotted to show correlation across the MECO event (light orange box) and during the warming phase (dark orange box).

interval, between 83.29 and 75.66 mbsf, with two positive peaks between 70.28 and 69.00 mbsf that parallel the general BFAR trend.

Despite the wide range of CFAR values (>63 µm) (Figure 5), there is a short interval with low values between 74.77 and 71.63 mbsf, while above average (>0.5 g * cm^2/Kyr) values are constant in the lower and upper parts of the section. This proxy has been commonly used as an estimation of the planktonic foraminiferal ARs (e.g., Boscolo Galazzo et al., 2014).

4.5. Calcareous Nannofossil Biostratigraphy and Abundance Patterns

Calcareous nannofossil assemblages from Site 702 were previously reported by Pea (2011), but our data provide a biostratigraphic frame based on the semiquantitative abundance patterns of the index species (N/mm^2) used in the biozonations (Figure 6 and Table S4).

4.5.1. Base of *Reticulofenestra umbilicus* (>14 µm)

It marks the base of Subzone CP14a (Okada & Bukry, 1980) and the base of Zone NP16, as the Top of *Blackites gladius*, which was originally proposed to define the base of Zone NP16 (Martini, 1971), has been reported to extend into lower Zone NP17 (e.g., Agnini et al., 2014; Berggren & Aubry, 1984; Wei & Wise, 1989). *Reticulofenestra umbilicus* is present throughout the section with a continuous, relatively common abundance that is lower in the basal part and increases from 74.1 (±0.10) mbsf upward. This abundance pattern indicates that the base of this taxon is positioned below the base of the studied interval.

4.5.2. Base of *Cribrocentrum reticulatum*

It denotes the base of Zone CNE14 (Agnini et al., 2014). This taxon is unevenly distributed and suggests, conversely to what was reported in Pea (2011), that its base is located below the base of the study section. The appearance of *C. reticulatum* shows diachroneity, starting more than 2 Myr before at low-middle latitudes than at high latitudes (Agnini et al., 2014; Villa et al., 2008). This discrepancy and its low abundance at Site 702 are most likely related to the warm/temperate preference suggested for this taxon (e.g., Backman, 1987; Bukry, 1973; Haq & Lohmann, 1976).

4.5.3. Top of *Sphenolithus furcatolithoides*

It has been proposed to define the base of Subzone MNP16B (Fornaciari et al., 2010) at low-middle latitudes. This warm water taxon (e.g., Agnini et al., 2006; Gibbs et al., 2004; Wei & Wise, 1992) is rare at Site 702, and only one specimen was observed at 79.40 mbsf. This finding does not allow us to precisely position this biohorizon, but the specimen lies, as expected, between the base of *R. umbilicus* and the appearance of *Dictyococcites bisectus*.

4.5.4. Base of Common (Bc) and Continuous *Dictyococcites bisectus* (>10 μm)

It marks the base of Zone CNE15 (Agnini et al., 2014) at low-middle latitudes, while it is found to occur more than 2 Myr later in the high latitude Southern Ocean Site 748 (Villa et al., 2008). The taxonomy of *D. bisectus* is complicated, and we follow Agnini et al. (2014), who include forms >10 μm, in order to directly correlate results between Site 702 and low to low-middle latitude sites (i.e., Sites 1051 and 1052 and Alano section). Similar taxa such as *D.* aff. *bisectus* and *D. hesslandii* (see Agnini et al., 2014, for detail on taxonomy) enter or reenter in the record very close to each other in Chron C18r (Pea, 2011; Figure 6). These taxa are rare at Site 702 likely because of their temperate affinity (Haq & Lohmann, 1976; Villa et al., 2008; Wei & Wise, 1990), but they display a relatively continuous presence (Figure 6 and Table S4).

4.5.5. Top Common/Top of *Sphenolithus spiniger*

The top common of *S. spiniger* defines the base of Subzone MNP17A (Fornaciari et al., 2010). This warm water species is virtually absent in the lower part of the study interval at Site 702, and it displays a rare but substantially continuous occurrence from 73.05 (±0.05) mbsf to 70.80 (±0.1) mbsf, where it disappears. A similar trend for the final tail of occurrence of this taxon has been recognized in multiple sections at low-middle latitudes (e.g., Sites 1051, 1052, and 1263 and Alano, Italy; Fornaciari et al., 2010; Toffanin et al., 2011; Agnini et al., 2014).

4.5.6. Top of *Chiasmolithus solitus*

It marks the base of Zone NP17 and Subzone CP14b (Martini, 1971; Okada & Bukry, 1980). This species is continuously present across the study interval at Site 702, and its highest occurrence is located in the upper part. We cannot thus validate the inconsistencies reported in the literature on the relative position of this biohorizon among sequences located at low-middle latitudes and between high and low-middle latitudes sections (Agnini et al., 2014; Marino & Flores, 2002; Villa et al., 2008).

In summary, the simultaneous presence of *R. umbilicus* (>14 μm) and *C. solitus* indicates that the study interval belongs entirely to Subzone CP14a and Zone NP16 (Martini, 1971; Okada & Bukry, 1980). The presence of *C. reticulatum* from the base of the section and the appearance of *D. bisectus* at 73.20 (±0.1) mbsf indicate that the study interval spans the upper part of Zone CNE14 and the basal part of Zone CNE15 (Agnini et al., 2014).

The semiquantitative abundance patterns of selected taxa show major changes in surface waters across the study interval. The total number of forms ascribable to the genus *Sphenolithus*, which includes mainly *S. moriformis* gr., displays a remarkable increase in abundance at 74.80 (±0.10) mbsf and remains relatively high up to 70.80 (±0.10) mbsf, where it returns to the background values observed in the lower part. Similarly, the abundance of forms belonging to *Ericsonia formosa*, the only representative of its genus, increases exactly in the same interval. Within this interval but across a shorter period (from 73.95 ± 0.05 to 71.80 ± 0.10 mbsf), the genus *Discoaster* also shows an increase from virtually zero to a peak value of 50 specimens per mm^2 recorded at 72.80 mbsf. An anomalous and highly variable increase in abundance of *Zyghrablithus bijugatus* starts at 71.15 ± 0.15 mbsf, but the abundance pattern is characterized by a high variance of the signal ($1\sigma = 36$; Figure 6).

5. Discussion

5.1. Finding MECO

The MECO event has been defined by a negative bulk OIE, followed by a peak interval of lowest $\delta^{18}O$ values that ends with a rapid recovery to preexcursion values. This pattern is recurrent in records from different latitudes and ocean basins (Bohaty et al., 2009; Giorgioni et al., 2019; Jovane et al., 2007; Spofforth et al., 2010). At Site 702 in the South Atlantic Ocean, our high-resolution isotopic analyses follow the same overall trend. $\delta^{18}O$ profiles show a manifest decrease starting at 75 mbsf, followed by three relative minimum values at 72.15, 71.70, and 71 mbsf, ending in a rapid recovery (+0.6‰ $\delta^{18}O_{bulk}$ within 0.4 m) after the last minimum peak (Figure 3). Overall, the $\delta^{18}O_{bulk}$ pattern is paralleled by the $\delta^{18}O_{benthic}$ record, although the benthic record presents a positive excursion in the lower part of the studied interval, before the beginning of the OIE (Figure 3).

The driving mechanisms of the MECO are still largely unknown; however, the $\delta^{18}O_{bulk}$ versus $\delta^{13}C_{bulk}$ cross-plot suggests that these mechanisms were weaker or absent in surface waters before and after the

warming. Samples from the pre- and post-MECO periods show no correlation, while samples comprising the MECO event have a positive linear correlation (Figure S4a). Similarly, the $\delta^{18}O_{benthic}$ versus $\delta^{13}C_{benthic}$ cross-plot show no correlation in samples from the pre- and post-MECO interval (Figure S4b), suggesting that MECO driving mechanisms were weaker or absent before and after the MECO also in the deep sea. The positive correlation between $\delta^{18}O$ and $\delta^{13}C$ supports a constant linear relationship between temperature ($\delta^{18}O$) and carbon release ($\delta^{13}C$) across the MECO, as observed in older hyperthermal events (Lauretano et al., 2015, 2018; Stap et al., 2010; Westerhold et al., 2018). The linear regression calculated with benthic isotope samples across the MECO (dashed line Figure S4b) is less steep than those calculated for other early Eocene hyperthermals (Figure S4c; Westerhold et al., 2018), which suggests a different carbon signature and heavier carbon source of the MECO (Lauretano et al., 2015).

Comparison of our high-resolution stable isotope record with that from Site 1263 suggests a total duration of ~270 Kyr for the MECO (between the onset of the bulk OIE at 75 mbsf and the recovery to the same $\delta^{18}O_{bulk}$ values at 70.60 mbsf) (Figure 3). Site 1263, on which our age model is based, experienced some dissolution during the MECO peak, which may have led to slight overestimations of sedimentation rates across this interval. However, it seems very likely that the total duration of the MECO did not exceed 300 Kyr at Site 702. Conversely, if the duration of the MECO is calculated using the linear sedimentation rate data from the shipboard report (1.224 cm/Kyr across the study interval), its duration is >700 Kyr.

5.2. Paleoenvironmental Interpretation: Benthic Foraminiferal Response

Benthic foraminifera reveal short, transient changes in the assemblages that point to a temporary shift in environmental conditions at the seafloor across the study interval.

The species with larger relative abundance shifts belong to subcluster A1, which is mainly composed of phytodetritus exploiting taxa (PET; e.g., *A. weddellensis*, *Caucasina* sp., and *E. exigua*) and shows higher abundances in the middle of the studied interval, between 76.86 and 69.39 mbsf (Figure 4). PET taxa have been related to seasonality (Boscolo Galazzo et al., 2015, and references therein) and probably to an opportunistic life strategy and rapid reproduction due to their small size. Across this interval with high abundance of species from Subcluster A1, there are peaks in relative abundance of *B. huneri* (the main component of Subcluster A2; Figure 4), a species that has been associated with seasonality and input of refractory (low quality) organic matter (e.g., D'haenens et al., 2012). The interval with peaks in PET taxa and *B. huneri* (~76.5–69 mbsf) probably represents a period of stronger seasonality, with changes in the type of organic matter flux to the seafloor. High percentages of Subclusters A1 and A2 coincide with high $\delta^{13}C$ values (Figure 3), pointing to a change in the organic carbon source. The negative correlation between the abundance of Subclusters A1 and A2 may be related to their different ecological preferences, with species from Subcluster A1 adapted to feeding on phytodetritus and those from Subcluster A2 preferentially feeding on refractory organic matter. These results support fluctuations in the organic carbon flux across this interval.

Subclusters B1 and B2 decrease in relative abundance coinciding with the interval of increased percentage of Subclusters A1 and A2 (between ~76.5 and 72.5 mbsf; Figure 4). While subcluster B1 recovers to previous (and even higher) relative abundance values after this interval, subcluster B2 does show consistently low values. In addition, the ARs of *N. truempyi* (main component of Subcluster B1) show no significant changes across the studied interval and point to a decrease in relative-—but not in absolute—abundance (Figure 5). This nonspecialist, cosmopolitan epifaunal species and other Eocene lower bathyal species of Subcluster B1 (e.g., *Globocassidulina subglobosa*, *Oridorsalis umbonatus*, and *Bulimina alazanenesis*) might have adapted better than *B. elongata* to the inferred changes in organic matter flux, whose ARs notably fluctuate.

DCA analysis confirms differences among subclusters (Figure S8). Axis 1 may be controlled by the type of organic matter reaching the seafloor, with species from Cluster A (which thrived during the period of inferred changes in organic matter flux, 76.86–69.39 mbsf) showing positive values, and species from Cluster B, which dominated during the pre- and post-event, showing negative values. The interpretation of Axis 2 is more complex, but it might be related to changes in temperature. Species from Cluster A2, which is more abundant during the OIE (MECO warming phase), show high Axis 2 values, while the rest of the species have low or negative values along this axis.

The main limiting factors for deep-sea benthic foraminifera are oxygen concentration and the amount and type of food (e.g., Gooday, 2003; Murray, 2006). No evidence for low oxygenation has been found at Site 702 (e.g., species tolerant to low-oxygen conditions and dark sediments); thus, oxygen was not likely a significant factor driving the benthic turnover at this site. Assemblages are composed of mixed infaunal and epifaunal taxa, and the morphogroups ratio does not show any significant trends (Figure 4). Together with the assemblage composition (Figure S7), they point to fairly steady oligo-mesotrophic conditions at the seafloor. Continuously high (>80%) $CaCO_3$ content (Figure 5), the strong dominance of calcareous (>98%) over agglutinated benthic foraminifera, and the overall good preservation of the foraminiferal tests and the nannofossil assemblages (Pea, 2011; this study) indicate that Site 702 was well above the CCD across the MECO, as suggested by Bohaty et al. (2009).

No extinctions have been recorded across the MECO at Site 702 (Table S2) in contrast to the extinction of almost half of deep-sea benthic foraminiferal species across the PETM (e.g., Alegret et al., 2009, b, 2018; Arreguín-Rodríguez et al., 2018; Miller et al., 1987; Thomas, 1998, 2003, 2007; Tjalsma & Lohmann, 1983). Similarly, no benthic foraminiferal extinctions have been recorded across the MECO in other locations from different latitudes and basins (Boscolo Galazzo et al., 2013; Moebius et al., 2014, 2015) nor across some Paleocene (e.g., Alegret et al., 2016; Deprez et al., 2017) and Eocene smaller hyperthermal events (e.g., Arreguín-Rodríguez et al., 2016; Arreguín-Rodríguez & Alegret, 2016).

5.3. Paleoenvironmental Interpretation: Surface Waters

Previous studies on the paleoenvironmental affinities of calcareous nannofossil taxa have documented that *Discoaster* (e.g., Haq & Lohmann, 1976; Haq, Lohmann, & Sherwood, 1977; Haq, Premoli-Silva, Lohmann, 1977; Wei & Wise, 1990; Pospichal & Wise, 1990; Agnini et al., 2006), *Sphenolithus* (e.g., Agnini et al., 2007; Aubry, 1998; Bralower, 2002; Gibbs et al., 2004; Wei & Wise, 1990), and *Ericsonia* (e.g., Haq & Lohmann, 1976; Haq, Lohmann et al., 1977; Wei & Wise, 1990; Aubry, 1992; Wei & Wise, 1992; Kelly et al., 1996; Bralower, 2002; Agnini et al., 2007) preferentially thrive in warm waters and oligotrophic conditions. The virtual absence of these taxa in the lower and upper parts of the study interval, combined with their abundance peaks between 74.80 and 70.80 mbsf, suggest that they were ecologically excluded before and after the MECO because of the cool sea-surface temperatures at Site 702. Coinciding with the beginning of surface water warming and the OIE that marks the MECO, *Discoaster*, *Sphenolithus*, and *Ericsonia* extended their biogeographical distribution. Their abundance peaks suggest that the increase in surface-water temperature was sufficient to surmount their ecological thresholds. Anomalous warming allowed these taxa to survive within their thermal optimum but outside their natural biogeographical domain, while the disappearance of these species is related to decreased temperatures and increased nutrient availability. More interestingly, the biochronology of the appearances and disappearances of the marker species of standard zonations show that Site 702 was located at the transition between high and low-middle latitudes and could in fact represent the ideal link between these two apparently unconnected paleoecological domains. Understanding the different responses of calcareous nannofossils to the MECO at different latitudes is fundamental, as it could shed light on the appearance of *D. bisectus* and the evolution of sphenoliths at low-middle latitudes, as well as on the expansion of temperate taxa toward high latitudes (Toffanin et al., 2011; Villa et al., 2008, 2014). Site 702 records the expansion of warm water taxa and temperate taxa toward higher latitudes across the MECO, suggesting that a strong global teleconnection exists between these different geographical areas.

The peak of *Z. bijugatus* in the post-MECO interval may be related to a change in water chemistry rather than to temperature changes. Warming during the MECO should have favored the arrival and proliferation of this species, as documented for other warm water/oligotrophic taxa (Agnini et al., 2007). However, its increase during the post-MECO at Site 702 points to an intermittent carbonate oversaturation of sea surface waters, triggered by increased alkalinity due to accelerated terrestrial chemical weathering, as suggested for the PETM (Dickens et al., 1997; Penman & Zachos, 2018; Zeebe & Zachos, 2013). The record of these changes well after the climax of the MECO contributes to the MECO conundrum (Sluijs et al., 2013). Indeed, the extremely fragile structure of *Z. bijugatus* holococcolith is easily dissolved in the early stage of the sedimentation process, but the enhanced availability of carbonate in the seawaters might have favored the preservation of the very delicate crystallites forming the holococcolith.

5.4. Accummulation Rates and the Ocean Organic Carbon Budget

An increase in metabolic rates has been previously invoked to explain lower foraminiferal ARs across hyperthermal events (e.g., Boscolo Galazzo et al., 2015; Arreguín-Rodríguez et al., 2016). Higher temperatures increase the metabolic rates of heterotroph organisms such as planktonic and benthic foraminifera, requiring a higher nutrient intake (e.g., John et al., 2013; Laws et al., 2000). If the food demand increase is not compensated (e.g., by an increase in primary productivity), it could result in an overall decrease in heterotroph productivity (Boscolo Galazzo et al., 2014). Additionally, increased respiration rates throughout the water column may have contributed to decreasing organic carbon reaching the seafloor. Oligotrophic settings are more likely to display this mechanism and register lower benthic and planktonic foraminifera ARs across a warming period, as nutrient availability is already low and primary productivity is not able to cope with the increasing demand. This mechanism has been suggested for oligotrophic Site 1263 (Boscolo Galazzo et al., 2015), where low BFARs and CFARs are recorded during the MECO peak and might also explain the decreased BFARs and CFARs recorded at Site 702.

Our records show low CFARs values between 74.77 and 71.63 mbsf, coinciding with the duration of the MECO $\delta^{18}O_{bulk}$ excursion (Figure 3). Similarly, BFAR shows relatively low values from 74.42 mbsf upward, but it is between 72.72 mbsf and 70.58 where minimum values are reached. This period of low BFARs overlaps with the highest isotopic excursion rate of the $\delta^{18}O_{benthic}$ record (−0.74‰ in 1.86 m), during the later stage of MECO warming. Hence, CFAR and BFAR values at Site 702 seem to be coupled with $\delta^{18}O_{bulk}$ and $\delta^{18}O_{benthic}$ excursions, respectively, happening first in surface waters (CFAR values start to decrease at 74.77 mbsf) and right after in the deep sea (BFAR decreasing at 74.42 mbsf).

BFARs have been largely used as a proxy for delivery of organic matter to the seafloor (e.g., Diester-Haass & Faul, 2019). Low BFARs values have been recorded across MECO warming at Site 702 (this study) and during MECO peak conditions at Site 1263 (Boscolo Galazzo et al., 2015), suggesting less organic matter arriving to the seafloor in oligo-mesotrophic settings. This mechanism could have played a significant role as a positive feedback in the ocean carbon budget in the short term. If export productivity decreased during MECO warming (as reported by low CFARs) and less organic matter arrived at the seafloor (as reported by low BFARs), the organic carbon pump was likely less efficient during this warming period. As a consequence, less organic carbon was being buried at the seafloor (Diester-Haass & Faul, 2019); hence, this oceanic region would have been less efficient or slower taking up carbon from the atmosphere and favoring CO_2 accumulation in the ocean during warming. Although this mechanism accounts for the observed faunal changes at Sites 702 and 1263 and the decreased export productivity registered at Equatorial Atlantic ODP Site 959 (Cramwinckel et al., 2019), it does not apply to eutrophic settings (e.g., Site 1051, North Atlantic Ocean) where BFARs and CFARs increased during MECO peak conditions (Moebius et al., 2015). Further AR estimates, accompanied by revised sedimentation rates (calculated with robust age models), are needed to accurately assess foraminiferal ARs and their role in the ocean organic carbon budget during MECO warming.

5.5. Disentangling MECO Environmental Signal

Carbon stable isotopes have been challenging to interpret across the MECO due to the different trends revealed at several sites (Bohaty et al., 2009). At Site 702, the $\delta^{13}C_{bulk}$ record shows similarities with the $\delta^{18}O_{bulk}$ trend, in particular the three-peaked values at 72.15, 71.70, and 71 mbsf (Figure 3). This suggests a correlated mechanism during peak conditions for both isotope records, as shown by cross-plot linear regressions (Figure S4). Interestingly, a positive $\delta^{13}C_{bulk}$ excursion happening before the MECO OIE overlaps with the main shifts recorded in the benthic fauna. The start of the positive $\delta^{13}C_{bulk}$ excursion at 78.35 mbsf coincides with decreasing diversity of benthic assemblages (78.26 mbsf) (Figure 3). These shifts predate by 1.76 m (~150 Kyr) the start of the $\delta^{18}O_{bulk}$ excursion, which has traditionally marked the start of the MECO event. Sharp abundance increases of PET benthic taxa (Subcluster A1) as well as even lower diversity values are particularly noticeable between 76.86 and 72.46 mbsf, a period across which $\delta^{13}C_{bulk}$ reach higher values (Figure 2). As discussed in section 5.2, this period is likely associated with a change in the flux of organic matter, especially between 76.45–75.26 and 73.83–72.46 mbsf, which significantly affected the benthos (low diversity, high dominance, and maximum abundance of Subcluster A1). The relative and absolute abundance of *B. elongata* (main component of Subcluster B2) decrease across these two intervals (Figures 4 and 5) and its maximum length values decrease (Figure 4), suggesting that this species (and

likely the other species from Subcluster B2) was disadvantaged by changes in the type of food supply to the seafloor. Our results document that the significant ecological changes recorded by the benthic foraminifera assemblages, occurring ~150 Kyr before the start of the OIE, are coupled with a positive CIE. Carbon isotopic changes are hence likely related to changes in the organic carbon flux to the seafloor, as evidenced by benthic assemblages.

Regarding the oxygen isotope signal, warming started synchronously in both surface and bottom waters, similarly to Site 1263 records (Boscolo Galazzo et al., 2014) but contrasting with data at Site 738, where warming is recorded earlier at the bottom than at the surface (Bohaty et al., 2009). The extent of warming during MECO peak conditions appears to have lasted longer in surface waters than in the deep sea in the Indian sector of Southern Ocean Site 738 (Bohaty et al., 2009). Instead, our O isotope records from Site 702 show tightly coupled variations in bulk and benthic values across MECO peak conditions (Figure 3), suggesting a similar warming pace in both surface and bottom waters, mirroring the records at Site 1263 (Boscolo Galazzo et al., 2014). Environmental effects of the MECO at Site 702 were more similar to low latitude Atlantic Sites (Site 1263) than other sites at similar latitudes (e.g., Site 738) in the Southern Ocean (Indian sector). Calcareous nannofossil data support this hypothesis, suggesting that Site 702 temporarily became part of the low-middle latitude domain during the MECO. High-resolution records at other southern high latitude sites are needed to verify if warming started earlier in bottom waters in the western part of the Southern Ocean and to assess the duration of MECO peak conditions in surface and bottom waters.

6. Conclusions

New high-resolution carbon and oxygen isotopic records in bulk carbonate and monospecific benthic foraminifera at ODP Site 702 yield a ~300 Kyr duration of the MECO event in the South Atlantic. The mechanisms driving coupled changes in $\delta^{18}O$ and $\delta^{13}C$ isotope values were weaker or absent before and after the event according to linear regression analysis of the $\delta^{18}O$ versus $\delta^{13}C$ cross-plots.

We document the expansion of warm and temperate calcareous nannofossil taxa toward higher latitudes during the MECO at Site 702, suggesting a strong global teleconnection between these different biogeographical areas. In the deep sea, changes in the benthic fauna predate by ~150 Kyr the start of the warming and correlate with a positive $\delta^{13}C$ excursion, pointing to a change in the type of organic matter reaching the seafloor prior to MECO warming. Planktonic and BFARs decline during warming, which could have act as a positive feedback during MECO warming due to decreased export productivity and decreased organic carbon burial at Site 702 and other ocean oligotrophic ocean settings.

Acknowledgments
We thank M. Cramwinckel, V. Luciani, and Associate Editor P. Lippert for their thoughtful comments that helped improving this manuscript. We also thank Henning and his team for isotope analyses at MARUM, Holger and Alex for sampling assistance at BCR, and Cristina for SEM imaging at Servicio General de Apoyo a la Investigación-SAI, Universidad de Zaragoza. Samples and data used in this research were provided by the International Ocean Discovery Program (IODP), which is sponsored by the U.S. National Science Foundation (NSF) and participating countries. L. R. C. and L. A. financial support provided by the Spanish Ministry of Economy and Competitiveness (Project CGL 2017-84693-R), IUCA (Instituto Universitario de Investigación en Ciencias Ambientales de Aragón), and Aragon government (Reference Group E33_17R) co-financed with Feder 2014-2020 "Building Europe from Aragon." E. D. and T. W. are supported by the Deutsche Forschungsgemeinschaft DFG Grants DA 1757/2-1 and WE 5479/3. Data reported are tabulated in the supporting information and archived in Pangaea database (https://doi.org/10.1594/PANGAEA.908747). This research is part of the PhD thesis of the first author.

References

Agnini, C., Fornaciari, E., Raffi, I., Catanzariti, R., Pälike, H., Backman, J., & Rio, D. (2014). Biozonation and biochronology of Paleogene calcareous nannofossils from low and middle latitudes. *Newsletters on Stratigraphy*, *47*(2), 131–181. https://doi.org/10.1127/0078-0421/2014/0042

Agnini, C., Fornaciari, E., Rio, D., Tateo, F., Backman, J., & Giusberti, L. (2007). Responses of calcareous nannofossil assemblages, mineralogy and geochemistry to the environmental perturbations across the Paleocene/Eocene boundary in the Venetian Pre-Alps. *Marine Micropaleontology*, *63*(1–2), 19–38. https://doi.org/10.1016/j.marmicro.2006.10.002

Agnini, C., Muttoni, G., Kent, D. V., & Rio, D. (2006). Eocene biostratigraphy and magnetic stratigraphy from Possagno, Italy: The calcareous nannofossil response to climate variability. *Earth and Planetary Science Letters*, *241*(3–4), 815–830. https://doi.org/10.1016/j.epsl.2005.11.005

Agnini, C., Spofforth, D. J. A., Dickens, G. R., Rio, D., Pälike, H., Backman, J., et al. (2016). Stable isotope and calcareous nannofossil assemblage record of the late Paleocene and early Eocene (Cicogna section). *Climate of the Past*, *12*(4), 883–909. https://doi.org/10.5194/cp-12-883-2016

Alegret, L., Ortiz, S., Arreguín-Rodríguez, G. J., Monechi, S., Millán, I., & Molina, E. (2016). Microfossil turnover across the uppermost Danian at Caravaca, Spain: Paleoenvironmental inferences and identification of the latest Danian event. *Palaeogeography, Palaeoclimatology, Palaeoecology*, *463*, 45–59. https://doi.org/10.1016/j.palaeo.2016.09.013

Alegret, L., Ortiz, S., & Molina, E. (2009). Extinction and recovery of benthic foraminifera across the Paleocene–Eocene Thermal Maximum at the Alamedilla section (Southern Spain). *Palaeogeography, Palaeoclimatology, Palaeoecology*, *279*(3–4), 186–200. https://doi.org/10.1016/j.palaeo.2009.05.009

Alegret, L., Ortiz, S., Orue-Etxebarria, X., Bernaola, G., Baceta, J. I., Monechi, S., et al. (2009). The Paleocene-Eocene Thermal Maximum: New data on microfossil turnover at the Zumaia Section, Spain. *PALAIOS*, *24*(5), 318–328. https://doi.org/10.2110/palo.2008.p08-057r

Alegret, L., Reolid, M., & Vega Pérez, M. (2018). Environmental instability during the latest Paleocene at Zumaia (Basque-Cantabric Basin): The bellwether of the Paleocene-Eocene Thermal Maximum. *Palaeogeography, Palaeoclimatology, Palaeoecology*, *497*, 186–200. https://doi.org/10.1016/j.palaeo.2018.02.018

Arndt, S., Jørgensen, B. B., LaRowe, D. E., Middelburg, J. J., Pancost, R. D., & Regnier, P. (2013). Quantifying the degradation of organic matter in marine sediments: A review and synthesis. *Earth-Science Reviews*, *123*, 53–86. https://doi.org/10.1016/j.earscirev.2013.02.008

Arreguín-Rodríguez, G. J., & Alegret, L. (2016). Deep-sea benthic foraminiferal turnover across early Eocene hyperthermal events at Northeast Atlantic DSDP Site 550. *Palaeogeography, Palaeoclimatology, Palaeoecology*, *451*, 62–72. https://doi.org/10.1016/j.palaeo.2016.03.010

Arreguín-Rodríguez, G. J., Alegret, L., & Thomas, E. (2016). Late Paleocene-middle Eocene benthic foraminifera on a Pacific seamount (Allison Guyot, ODP Site 865): Greenhouse climate and superimposed hyperthermal events: Benthic Foraminifera on Pacific seamount. *Paleoceanography*, *31*(3), 346–364. https://doi.org/10.1002/2015PA002837

Arreguín-Rodríguez, G. J., Thomas, E., D'haenens, S., Speijer, R. P., & Alegret, L. (2018). Early Eocene deep-sea benthic foraminiferal faunas: Recovery from the Paleocene Eocene Thermal Maximum extinction in a greenhouse world. *PLoS ONE*, *13*(2), e0193167. https://doi.org/10.1371/journal.pone.0193167

Aubry, M.-P. (1992). Late Paleogene calcareous nannoplankton evolution: A tale of climatic deterioration. In D. R. Prothero & W. A. Berggren (Eds.), *Eocene-Oligocene climatic and biotic evolution* (pp. 272–309). New Jersey: Princeton University Press. https://doi.org/10.1515/9781400862924.272

Aubry, M.-P. (1998). Early Paleogene calcareous nannoplankton evolution: A tale of climatic amelioration. In M.-P. Aubry, S. G. Lucas, & W. A. Berggren (Eds.), *Late Paleocene–early Eocene biotic and climatic events in the marine and terrestrial records* (pp. 158–201). New York: Columbia University Press.

Backman, J. (1987). Quantitative calcareous nannofossil biochronology of Middle Eocene through Early Oligocene sediment from DSDP Sites 522 and 523. In *Abhandlungen der Geologischen Bundesanstalt* (Vol. 39, pp. 21–31).

Backman, J., & Shackleton, N. J. (1983). Quantitative biochronology of Pliocene and early Pleistocene calcareous nannoplankton from the Atlantic, Indian and Pacific Oceans. *Marine Micropaleontology*, *8*, 141–170. https://doi.org/10.1016/0377-8398(83)90009-9

Berggren, W. A., & Aubry, M.-P. (1984). Rb-Sr glauconite isochron of the Eocene Castle Hayne Limestone, North Carolina: Further discussion. *Geological Society of America Bulletin*, *95*, 364–370. https://doi.org/10.1130/0016-7606(1984)95<364:rgiote>2.0.co;2

Berggren, W. A., & Pearson, P. N. (2005). A revised tropical to subtropical Paleogene planktonic foraminiferal zonation. *The Journal of Foraminiferal Research*, *35*(4), 279–298. https://doi.org/10.2113/35.4.279

Bijl, P. K., Houben, A. J. P., Schouten, S., Bohaty, S. M., Sluijs, A., Reichart, G.-J., et al. (2010). Transient Middle Eocene Atmospheric CO_2 and Temperature Variations. *Science*, *330*(6005), 819–821. https://doi.org/10.1126/science.1192534

Bohaty, S. M., & Zachos, J. C. (2003). Significant Southern Ocean warming event in the late middle Eocene. *Geology*, *31*(11), 1017–1020. https://doi.org/10.1130/G19800.1

Bohaty, S. M., Zachos, J. C., Florindo, F., & Delaney, M. L. (2009). Coupled greenhouse warming and deep-sea acidification in the middle Eocene. *Paleoceanography*, *24*(2), PA2207. https://doi.org/10.1029/2008PA001676

Bornmalm, L. (1997). *Taxonomy and paleoecology of late Neogene benthic foraminifera from the Caribbean Sea and eastern equatorial Pacific Ocean*. Oslo: Scandinavian Univ. Press.

Boscolo Galazzo, F., Giusberti, L., Luciani, V., & Thomas, E. (2013). Paleoenvironmental changes during the Middle Eocene Climatic Optimum (MECO) and its aftermath: The benthic foraminiferal record from the Alano section (NE Italy). *Palaeogeography, Palaeoclimatology, Palaeoecology*, *378*, 22–35. https://doi.org/10.1016/j.palaeo.2013.03.018

Boscolo Galazzo, F., Thomas, E., Pagani, M., Warren, C., Luciani, V., & Giusberti, L. (2014). The middle Eocene climatic optimum (MECO): A multiproxy record of paleoceanographic changes in the southeast Atlantic (ODP Site 1263, Walvis Ridge): MECO repercussions in the SE Atlantic. *Paleoceanography*, *29*(12), 1143–1161. https://doi.org/10.1002/2014PA002670

Bown, P., & Young, J. (1998). Techniques. In P. R. Bown (Ed.), *Calcareous nannofossil biostratigraphy* (pp. 16–28). Cambridge: Chapman & Hall.

Bralower, T. J. (2002). Evidence of surface water oligotrophy during the Paleocene-Eocene thermal maximum: Nannofossil assemblage data from Ocean Drilling Program Site 690, Maud Rise, Weddell Sea. *Paleoceanography*, *17*(2), 1029–1042. https://doi.org/10.1029/2001PA000662

Bukry, D. (1973). Low-latitude coccolith biostratigraphic zonation. In N. T. Edgar, & J. B. Saunders (Eds.), *Proceedings of the Ocean Drilling Program, Initial Reports* (Vol. 15, pp. 685–703). College Station, Texas: Ocean Drilling Program. https://doi.org/10.2973/dsdp.proc.15.1973

Ciesielski, P. F., & Kristoffersen, Y. (1988). *Proceedings of the Ocean Drilling Program, Initial Reports* (Vol. 114). College Station, Texas: Ocean Drilling Program.

Ciesielski, P. F., & Kristoffersen, Y. (1991). *Proceedings of the Ocean Drilling Program, Scientific Results* (Vol. 114). College Station, Texas: Ocean Drilling Program.

Clement, B. M., & Hailwood, E. A. (1991). Magnetostratigraphy of sediments from Sites 701 and 702. In P. F. Ciesielski, & Y. Kristoffersen (Eds.), *Proceedings of the Ocean Drilling Program, Scientific Results* (Vol. 114, pp. 359–366). https://doi.org/10.2973/odp.proc.sr.114.1991

Corliss, B. H. (1991). Morphology and microhabitat preferences of benthic foraminifera from the northwest Atlantic Ocean. *Marine Micropaleontology*, *17*(3–4), 195–236. https://doi.org/10.1016/0377-8398(91)90014-W

Corliss, B. H., & Chen, C. (1988). Morphotype patterns of Norwegian Sea deep-sea benthic foraminifera and ecological implications. *Geology*, *16*(8), 716–719. https://doi.org/10.1130/0091-7613

Cramwinckel, M. J., van der Ploeg, R., Bijl, P. K., Peterse, F., Bohaty, S. M., Röhl, U., et al. (2019). Harmful algae and export production collapse in the equatorial Atlantic during the zenith of Middle Eocene Climatic Optimum warmth. *Geology*, *47*, 247–250. https://doi.org/10.1130/G45614.1

Deprez, A., Jehle, S., Bornemann, A., & Speijer, R. P. (2017). Differential response at the seafloor during Palaeocene and Eocene ocean warming events at Walvis Ridge, Atlantic Ocean (ODP Site 1262). *Terra Nova*, *29*(1), 71–76. https://doi.org/10.1111/ter.12250

D'haenens, S., Bornemann, A., Stassen, P., & Speijer, R. P. (2012). Multiple early Eocene benthic foraminiferal assemblage and δ13C fluctuations at DSDP Site 401 (Bay of Biscay—NE Atlantic). *Marine Micropaleontology*, *88–89*, 15–35. https://doi.org/10.1016/j.marmicro.2012.02.006

Dickens, G. R., Castillo, M. M., & Walker, J. C. G. (1997). A blast of gas in the latest Paleocene: Simulating first-order effects of massive dissociation of oceanic methane hydrate. *Geology*, *25*(3), 259–262. https://doi.org/10.1130/0091-7613(1997)025%3C0259:ABOGIT%3E2.3.CO;2

Diester-Haass, L. (1995). Middle Eocene to early Oligocene paleoceanography of the Antarctic Ocean (Maud Rise, ODP Leg 113, Site 689): Change from a low to a high productivity ocean. *Palaeogeography, Palaeoclimatology, Palaeoecology*, *113*(2–4), 311–334. https://doi.org/10.1016/0031-0182(95)00067-V

Diester-Haass, L., & Faul, K. (2019). Paleoproductivity reconstructions for the Paleogene Southern Ocean: A direct comparison of geochemical and micropaleontological proxies. *Paleoceanography and Paleoclimatology*. https://doi.org/10.1029/2018PA003384

Edgar, K. M., Wilson, P. A., Sexton, P. F., Gibbs, S. J., Roberts, A. P., & Norris, R. D. (2010). New biostratigraphic, magnetostratigraphic and isotopic insights into the Middle Eocene Climatic Optimum in low latitudes. *Palaeogeography, Palaeoclimatology, Palaeoecology*, *297*(3–4), 670–682. https://doi.org/10.1016/j.palaeo.2010.09.016

Edgar, K. M., Wilson, P. A., Sexton, P. F., & Suganuma, Y. (2007). No extreme bipolar glaciation during the main Eocene calcite compensation shift. *Nature*, *448*(7156), 908–911. https://doi.org/10.1038/nature06053

Fisher, R. (1953). Dispersion on a sphere. *Proceedings of the Royal Society A: Mathematical, Physical and Engineering Sciences*, *217*(1130), 295–305. https://doi.org/10.1098/rspa.1953.0064

Fontanier, C., Jorissen, F. J., Licari, L., Alexandre, A., Anschutz, P., & Carbonel, P. (2002). Live benthic foraminiferal faunas from the Bay of Biscay: Faunal density, composition, and microhabitats. *Deep Sea Research Part I: Oceanographic Research Papers*, *49*(4), 751–785. https://doi.org/10.1016/S0967-0637(01)00078-4

Fornaciari, E., Agnini, C., Catanzariti, R., Rio, D., Bolla, E. M., & Valvasoni, E. (2010). Mid-Latitude calcareous nannofossil biostratigraphy and biochronology across the middle to late Eocene transition. *Stratigraphy*, *7*, 229–264. EID: 2-s2.0-79953076907

Galazzo, F. B., Thomas, E., & Giusberti, L. (2015). Benthic foraminiferal response to the Middle Eocene Climatic Optimum (MECO) in the South-Eastern Atlantic (ODP Site 1263). *Palaeogeography, Palaeoclimatology, Palaeoecology*, *417*, 432–444. https://doi.org/10.1016/j.palaeo.2014.10.004

Gibbs, S., Shackleton, N., & Young, J. (2004). Orbitally forced climate signals in mid-Pliocene nannofossil assemblages. *Marine Micropaleontology*, *51*(1–2), 39–56. https://doi.org/10.1016/j.marmicro.2003.09.002

Giorgioni, M., Jovane, L., Rego, E. S., Rodelli, D., Frontalini, F., Coccioni, R., et al. (2019). Carbon cycle instability and orbital forcing during the Middle Eocene Climatic Optimum. *Scientific Reports*, *9*(1), 9357. https://doi.org/10.1038/s41598-019-45763-2

Gooday, A. J. (2003). Benthic foraminifera (protista) as tools in deep-water palaeoceanography: Environmental influences on faunal characteristics. *Advances in Marine Biology*, *46*. https://doi.org/10.1016/S0065-2881(03)46002-1

Gooday, A. J., & Rathburn, A. E. (1999). Temporal variability in living deep-sea benthic foraminifera: A review. *Earth-Science Reviews*, *46*(1–4), 187–212. https://doi.org/10.1016/S0012-8252(99)00010-0

Gordon, A. L., Georgi, D. T., & Taylor, H. W. (1977). Antarctic polar front zone in the Western Scotia Sea—Summer 1975. *Journal of Physical Oceanography*, *7*, 309–328. https://doi.org/10.1175/1520-0485(1977)007<0309:apfzit>2.0.co;2

Gradstein, F. M., Ogg, J. G., Schmitz, M., & Ogg, G. (2012). *The geologic time Scale 2012 2-Volume set*. Elsevier Science. https://doi.org/10.1016/C2011-1-08249-8

Gross, O. (2000). Influence of temperature, oxygen and food availability on the migrational activity of bathyal benthic foraminifera: Evidence by microcosm experiments. In G. Liebezeit, S. Dittmann, & I. Kröncke (Eds.), *Life at interfaces and under extreme conditions* (pp. 123–137). Dordrecht: Springer Netherlands. https://doi.org/10.1007/978-94-011-4148-2_12

Hammer, Ø., & Harper, D. (2005). *Paleontological data analysis*. Oxford: Blackwell Publishing.

Hammer, Ø., Harper, D. A. T., & Ryan, P. D. (2001). PAST: Paleontological statistics software package for education and data analysis. *Paleontologia Electronica*, *4*(1), 9. https://palaeo-electronica.org/2001_1/past/issue1_01.htm

Haq, B. U., & Lohmann, G. P. (1976). Early Cenozoic calcareous nannoplankton biogeography of the Atlantic Ocean. *Marine Micropaleontology*, *51*, 119–194. https://doi.org/10.1016/0377-8398(76)90008-6

Haq, B. U., Premoli-Silva, I., & Lohmann, G. P. (1977). Calcareous plankton paleobiogeographic evidence for major climatic fluctuations in the early Cenozoic Atlantic Ocean. *Journal of Geophysical Research*, *82*(27), 3861–3876. https://doi.org/10.1029/JC082i027p03861

Haq, B. U., Lohmann, G. P., & Sherwood, W. W. Jr. (1977). Calcareous nannoplankton biogeography and its paleoclimate implications: Cenozoic of the Falkland Plateau (DSDP Leg 36) and Miocene of the Atlantic Ocean. In P. F. Barker & I. W. D. Dalziel (Eds.), *Proceedings of the Ocean Drilling Program, Scientific Results* (Chap. 14, Vol. 36). College Station, Texas: Ocean Drilling Program. https://doi.org/10.2973/dsdp.proc.36.1977

Hayward, B. W., Kawagata, S., Sabaa, A., Grenfell, H., Van Kerckhoven, L., Johnson, K., & Thomas, E. (2012). *The last global extinction (Mid-Pleistocene) of deep-sea benthic foraminifera (Chrysalogoniidae, Ellipsoidinidae, Glandulonodosariidae, Plectofrondicularіidae, Pleurostomellidae, Stilostomellidae), their Late Cretaceous-Cenozoic history and taxonomy* (Vol. 43). Cushman Foundation for Foraminiferal Research Special Publication.

Herguera, J. C., & Berger, W. H. (1991). Paleoproductivity from benthic foraminifera abundance: Glacial to postglacial change in the west-equatorial Pacific. *Geology*, *19*, 1173–1176. https://doi.org/10.1130/0091-7613(1991)019<1173:PFBFAG>2.3.CO;2

Hilting, A. K., Kump, L. R., & Bralower, T. J. (2008). Variations in the oceanic vertical carbon isotope gradient and their implications for the Paleocene-Eocene biological pump. *Paleoceanography*, *23*(3). https://doi.org/10.1029/2007PA001458

Holbourn, A., Henderson, A. S., & MacLeod, N. (2013). *Atlas of benthic foraminifera*. Natural History Museum, London: Wiley-Blackwell.

Ivany, L. C., Lohmann, K. C., Hasiuk, F., Blake, D. B., Glass, A., Aronson, R. B., & Moody, R. M. (2008). Eocene climate record of a high southern latitude continental shelf: Seymour Island, Antarctica. *Geological Society of America Bulletin*, *120*(5–6), 659–678. https://doi.org/10.1130/B26269.1

John, E. H., Pearson, P. N., Coxall, H. K., Birch, H., Wade, B. S., & Foster, G. L. (2013). Warm ocean processes and carbon cycling in the Eocene. *Philosophical Transactions of the Royal Society A: Mathematical, Physical and Engineering Sciences*, *371*(2001), 20130099–20130099. https://doi.org/10.1098/rsta.2013.0099

Jones, R. W., & Charnock, M. A. (1985). "Morphogroups" of agglutinated foraminifera. Their life positions and feeding habits and potential applicability in (paleo)ecological studies. *Revue de Paléobiologie*, *4*(2), 311–320.

Jorissen, F. J. (1999). Benthic foraminiferal microhabitats below the sediment-water interface. In B. K. Sen Gupta (Ed.), *Modern foraminifera* (pp. 161–179). Dordrecht: Springer Netherlands. https://doi.org/10.1007/0-306-48104-9_10

Jorissen, F. J., de Stigter, H. C., & Widmark, J. G. (1995). A conceptual model explaining benthic foraminiferal microhabitats. *Marine Micropaleontology*, *26*(1–4), 3–15. https://doi.org/10.1016/0377-8398(95)00047-X

Jorissen, F. J., Fontanier, C., & Thomas, E. (2007). Chapter seven: Paleoceanographical proxies based on deep-sea benthic foraminiferal assemblage characteristics. In *Developments in marine geology* (Vol. 1, pp. 263–325). Elsevier. https://doi.org/10.1016/S1572-5480(07)01012-3

Jovane, L., Florindo, F., Coccioni, R., Dinares-Turell, J., Marsili, A., Monechi, S., et al. (2007). The middle Eocene climatic optimum event in the Contessa Highway section, Umbrian Apennines, Italy. *Geological Society of America Bulletin*, *119*(3–4), 413–427. https://doi.org/10.1130/B25917.1

Kelly, D. C., Bralower, T. J., Zachos, J. C., Silva, I. P., & Thomas, E. (1996). Rapid diversification of planktonic foraminifera in the tropical Pacific (ODP Site 865) during the late Paleocene thermal maximum. *Geology*, *24*, 423–426. https://doi.org/10.1130/0091-7613(1996)024<0423:RDOPFI>2.3.CO;2

Kirschvink, J. L. (1980). The least-squares line and plane and the analysis of palaeomagnetic data. *Geophysical Journal International*, *62*(3), 699–718. https://doi.org/10.1111/j.1365-246X.1980.tb02601.x

Laskar, J., Fienga, A., Gastineau, M., & Manche, H. (2011). La2010: A new orbital solution for the long term motion of the Earth. *Astronomy & Astrophysics*, *532*, A89. https://doi.org/10.1051/0004-6361/201116836

Lauretano, V., Littler, K., Polling, M., Zachos, J. C., & Lourens, L. J. (2015). Frequency, magnitude and character of hyperthermal events at the onset of the Early Eocene Climatic Optimum. *Climate of the Past*, *11*(10), 1313–1324. https://doi.org/10.5194/cp-11-1313-2015

Lauretano, V., Zachos, J. C., & Lourens, L. J. (2018). Orbitally paced carbon and deep-sea temperature changes at the peak of the early Eocene climatic optimum. *Paleoceanography and Paleoclimatology*, *33*, 1050–1065. https://doi.org/10.1029/2018PA003422

Laws, E. A., Falkowski, P. G., Smith, W. O., Ducklow, H., & McCarthy, J. J. (2000). Temperature effects on export production in the open ocean. *Global Biogeochemical Cycles*, *14*, 1231–1246. https://doi.org/10.1029/1999GB001229

Loeblich, A. R. Jr., & Tappan, H. (1987). *Foraminiferal genera and their classification* (Vol. 1-2). Van Nostrand Reinhold Company.

Luciani, V., Giusberti, L., Agnini, C., Fornaciari, E., Rio, D., Spofforth, D. J. A., & Pälike, H. (2010). Ecological and evolutionary response of Tethyan planktonic foraminifera to the middle Eocene climatic optimum (MECO) from the Alano section (NE Italy). *Palaeogeography, Palaeoclimatology, Palaeoecology*, *292*, 82–95. https://doi.org/10.1016/j.palaeo.2010.03.029

Lurcock, P. C., & Wilson, G. S. (2012). PuffinPlot: A versatile, user-friendly program for paleomagnetic analysis. *Geochemistry, Geophysics, Geosystems*, *13*, 1–6. https://doi.org/10.1029/2012GC004098

Lyle, M., Lyle, A. O., Backman, J., & Tripati, A. K. (2005). Biogenic sedimentation in the Eocene equatorial Pacific—The stuttering greenhouse and Eocene carbonate compensation depth. *Proceedings. Ocean Drilling Program. Scientific Results*, *199*, 1–35. https://doi.org/10.2973/odp.proc.sr.199.219.2005

Marino, M., & Flores, J.-A. (2002). Data report: Calcareous nannofossil data from the Eocene to Oligocene, Leg 177, Hole 1090B. In R. Gersonde, D. A. Hodell, & P. Blum (Eds.), *Proceedings of the Ocean Drilling Program, Scientific Results* (Chap. 8, Vol. 177). College Station, Texas: Ocean Drilling Program. https://doi.org/10.2973/odp.proc.sr.177.2003

Martini, E. (1971). Standard Tertiary and Quaternary calcareous nannoplankton zonation. In *Paper presented at 2nd International Conference Planktonic Microfossils, Rome, Italy* (pp. 739–785).

McFadden, P. L., & Reid, A. B. (1982). Analysis of palaeomagnetic inclination data. *Geophysical Journal International*, *69*, 307–319. https://doi.org/10.1111/j.1365-246X.1982.tb04950.x

Miller, K. G., Fairbanks, R. G., & Mountain, G. S. (1987). Tertiary oxygen isotope synthesis, sea level history, and continental margin erosion. *Paleoceanography*, *2*(1), 1–19. https://doi.org/10.1029/PA002i001p00001

Moebius, I., Friedrich, O., Edgar, K. M., & Sexton, P. F. (2015). Episodes of intensified biological productivity in the subtropical Atlantic Ocean during the termination of the Middle Eocene Climatic Optimum (MECO): Intensified productivity during the MECO. *Paleoceanography*, *30*(8), 1041–1058. https://doi.org/10.1002/2014PA002673

Moebius, I., Friedrich, O., & Scher, H. D. (2014). Changes in Southern Ocean bottom water environments associated with the Middle Eocene Climatic Optimum (MECO). *Palaeogeography, Palaeoclimatology, Palaeoecology*, *405*, 16–27. https://doi.org/10.1016/j.palaeo.2014.04.004

Mullender, T. A. T., Frederichs, T., Hilgenfeldt, C., de Groot, L. V., Fabian, K., & Dekkers, M. J. (2016). Automated paleomagnetic and rock magnetic data acquisition with an in-line horizontal "2G" system. *Geochemistry, Geophysics, Geosystems*, *17*, 1–14. https://doi.org/10.1002/2016GC006436

Müller-Merz, E., & Oberhänsli, H. (1991). Eocene bathyal and abyssal benthic foraminifera from a South Atlantic transect at 20–30 S. *Palaeogeography, Palaeoclimatology, Palaeoecology*, *83*(1–3), 117–171. https://doi.org/10.1016/0031-0182(91)90078-6

Murray, J. W. (1991). *Ecology and paleoecology of benthic foraminifera*. Longman.

Murray, J. W. (2006). *Ecology and applications of benthic foraminifera*. Cambridge University Press.

Okada, H., & Bukry, D. (1980). Supplementary modification and introduction of code numbers to the low-latitude coccolith biostratigraphic zonation (Bukry, 1973; 1975). *Marine Micropaleontology*, *5*, 321–325. https://doi.org/10.1016/0377-8398(80)90016-X

Ortiz, S., & Thomas, E. (2006). Lower-middle Eocene benthic foraminifera from the Fortuna section (Betic Cordillera, southeastern Spain). *Micropaleontology*, *52*(2), 97–150. https://doi.org/10.2113/gsmicropal.52.2.97

Pea, L. (2011). *Eocene-Oligocene paleoceanography of the subantarctic South Atlanctic: Calcareous nannofossil reconstructions of temperature, nutrient, and dissolution history*. University of Parma.

Penman, D. E., & Zachos, J. C. (2018). New constraints on massive carbon release and recovery processes during the Paleocene-Eocene Thermal Maximum. *Environmental Research Letters*, *13*(10), 105008. https://doi.org/10.1088/1748-9326/aae285

Perch-Nielsen, K. (1985). Cenozoic calcareous nannofossils. In H. M. Bolli, J. B. Saunders, & K. Perch-Nielsen (Eds.), *Plankton stratigraphy* (pp. 427–554). Cambridge University Press.

Pospichal, J. J., & Wise, S. W. Jr. (1990). Paleocene to middle Eocene calcareous nannofossils of ODP Sites 689 and 690, Maud Rise, Weddell Sea. In *Proceedings of the Ocean Drilling Program, Scientific Results* (Vol. 113, pp. 613–638). College Station, Texas: Ocean Drilling Program.

Reid, J. L., Nowlin, W. D. J., & Patzert, W. C. (1977). On the characteristics and circulation of the Southwestern Atlantic Ocean. *Journal of Physical Oceanography*, *7*, 62–91. https://doi.org/10.1175/1520-0485(1977)007<0062:otcaco>2.0.co;2

Sexton, P. F., Wilson, P. A., & Norris, R. D. (2006). Testing the Cenozoic multisite composite $\delta^{18}O$ and $\delta^{13}C$ curves: New monospecific Eocene records from a single locality, Demerara Rise (Ocean Drilling Program Leg 207). *Paleoceanography*, *21*(2), PA2019. https://doi.org/10.1029/2005PA001253

Sluijs, A., Zeebe, R. E., Bijl, P. K., & Bohaty, S. M. (2013). A middle Eocene carbon cycle conundrum. *Nature Geoscience*, *6*(6), 429–434. https://doi.org/10.1038/ngeo1807

Spofforth, D. J. A., Agnini, C., Pälike, H., Rio, D., Fornaciari, E., Giusberti, L., et al. (2010). Organic carbon burial following the middle Eocene climatic optimum in the central western Tethys. *Paleoceanography*, *25*(3), PA3210. https://doi.org/10.1029/2009PA001738

Stap, L., Lourens, L. J., Thomas, E., Sluijs, A., Bohaty, S., & Zachos, J. C. (2010). High-resolution deep-sea carbon and oxygen isotope records of Eocene Thermal Maximum 2 and H2. *Geology*, *38*, 607–610. https://doi.org/10.1130/G30777.1

Takata, H., Nomura, R., Tsujimoto, A., Khim, B.-K., & Chung, I. K. (2013). Abyssal benthic foraminifera in the eastern equatorial Pacific (IODP EXP 320) during the middle Eocene. *Journal of Paleontology*, *87*(06), 1160–1185. https://doi.org/10.1666/12-107

Tauxe, L., Stickley, C. E., Sugisaki, S., Bijl, P. K., Bohaty, S. M., Brinkhuis, H., et al. (2012). Chronostratigraphic framework for the IODP Expedition 318 cores from the Wilkes Land Margin: Constraints for paleoceanographic reconstruction. *Paleoceanography*, *27*, PA2214. https://doi.org/10.1029/2012PA002308

Thomas, E. (1998). The biogeography of the Late Paleocene benthic foraminiferal extinction. In M. P. Aubry, S. Lucas, & W. A. Berggren (Eds.), *Late Paleocene-Early Eocene biotic and climatic events in the marine and terrestrial records* (pp. 214–243). New York: Columbia University Press.

Thomas, E. (2003). Extinction and food at the seafloor: A high-resolution benthic foraminiferal record across the initial Eocene thermal maximum, Southern Ocean site 690. In *Special Paper 369: Causes and consequences of globally warm climates in the early Paleogene* (Vol. 369, pp. 319–332). Geological Society of America. https://doi.org/10.1130/0-8137-2369-8.319

Thomas, E. (2007). Cenozoic mass extinctions in the deep sea: What perturbs the largest habitat on Earth? In *Special Paper 424: Large Ecosystem Perturbations: Causes and Consequences* (Vol. 424, pp. 1–23). Geological Society of America. Retrieved from http://special-papers.gsapubs.org/cgi/doi/10.1130/2007.2424(01)

Tjalsma, R. C., & Lohmann, G. P. (1983). Paleocene-Eocene bathyal and abyssal benthic foraminifera from the Atlantic Ocean. *Micropaleontology*, Special Edition, *4*, 89.

Toffanin, F., Agnini, C., Rio, D., Acton, G., & Westerhold, T. (2013). Middle Eocene to early Oligocene calcareous nannofossil biostratigraphy at IODP Site U1333 (equatorial Pacific). *Micropaleontology*, *59*, 69–82. https://www.jstor.org/stable/24413317

Toffanin, F., Agnini, C., Fornaciari, E., Rio, D., Giusberti, L., Luciani, V., et al. (2011). Changes in calcareous nannofossil assemblages during the Middle Eocene Climatic Optimum: Clues from the central-western Tethys (Alano section, NE Italy). *Marine Micropaleontology*, *81*(1–2), 22–31. https://doi.org/10.1016/j.marmicro.2011.07.002

Tripati, A. (2005). Deep-sea temperature and circulation changes at the Paleocene-Eocene Thermal Maximum. *Science*, *308*(5730), 1894–1898. https://doi.org/10.1126/science.1109202

Van Morkhoven, F. P. C. M., Berggren, W. A., & Edwards, A. S. (1986). *Cenozoic cosmopolitan deep-water benthic foraminifera*. Elf-Aquitaine.

Villa, G., Fioroni, C., Pea, L., Bohaty, S., & Persico, D. (2008). Middle Eocene–late Oligocene climate variability: Calcareous nannofossil response at Kerguelen Plateau, Site 748. *Marine Micropaleontology*, *69*(2), 173–192. https://doi.org/10.1016/j.marmicro.2008.07.006

Villa, G., Fioroni, C., Persico, D., Roberts, A. P., & Florindo, F. (2014). Middle Eocene to Late Oligocene Antarctic glaciation/deglaciation and Southern Ocean productivity. *Paleoceanography*, *29*(3), 223–237. https://doi.org/10.1002/2013PA002518

Wade, B. S., & Kroon, D. (2002). Middle Eocene regional climate instability: Evidence from the western North Atlantic. *Geology*, *30*, 1011–1014. https://doi.org/10.1130/0091-7613(2002)030<1011:MERCIE>2.0.CO;2

Wei, W., & Thierstein, H. R. (1991). Upper Cretaceous and Cenozoic calcareous nannofossils of the Kerguelen Plateau (South Indian Ocean) and Prydz Bay (East Antarctica). In J. Barron, B. Larsen, et al. (Eds.), *Proceedings of the Ocean Drilling Program, Scientific Results* (Chap. 26, Vol. 119). College Station, Texas: Ocean Drilling Program. https://doi.org/10.2973/odp.proc.sr.119.1991

Wei, W., & Wise, S. W. J. (1989). Paleogene calcareous nannofossil magnetobiochronology: Results from South Atlantic DSDP Site 516. *Marine Micropaleontology*, *14*(1–3), 119–152. https://doi.org/10.1016/0377-8398(89)90034-0

Wei, W., & Wise, S. W. J. (1990). Biogeographic gradients of middle Eocene-Oligocene calcareous nannoplankton in the South Atlantic Ocean. *Palaeogeography, Palaeoclimatology, Palaeoecology*, *79*(1–2), 29–61. https://doi.org/10.1016/0031-0182(90)90104-F

Wei, W., & Wise, S. W. J. (1992). Eocene-Oligocene calcareous nannofossil magnetobiochronology of the Southern Ocean. *Newsletters on Stratigraphy*, *26*(2–3), 119–132. https://doi.org/10.1127/nos/26/1992/119

Westerhold, T., Röhl, U., Donner, B., & Zachos, J. C. (2018). Global extent of Early Eocene hyperthermal events—A new Pacific benthic foraminiferal isotope record from Shatsky Rise (ODP Site 1209). *Paleoceanography and Paleoclimatology*, *33*(6), 626–642. https://doi.org/10.1029/2017PA003306

Westerhold, T., Röhl, U., Frederichs, T., Agnini, C., Raffi, I., Zachos, J. C., & Wilkens, R. H. (2017). Astronomical calibration of the Ypresian timescale: Implications for seafloor spreading rates and the chaotic behavior of the solar system? *Climate of the Past*, *13*, 1129–1152. https://doi.org/10.5194/cp-13-1129-2017

Westerhold, T., Röhl, U., Frederichs, T., Bohaty, S. M., & Zachos, J. C. (2015). Astronomical calibration of the geological timescale: Closing the middle Eocene gap. *Climate of the Past*, *11*(9), 1181–1195. https://doi.org/10.5194/cp-11-1181-2015

Westerhold, T., Röhl, U., Pälike, H., Wilkens, R., Wilson, P. A., & Acton, G. (2014). Orbitally tuned timescale and astronomical forcing in the middle Eocene to early Oligocene. *Climate of the Past*, *10*(3), 955–973. https://doi.org/10.5194/cp-10-955-2014

Zachos, J. C. (2001). Trends, rhythms, and aberrations in global climate 65 Ma to present. *Science*, *292*(5517), 686–693. https://doi.org/10.1126/science.1059412

Zeebe, R. E., & Zachos, J. C. (2013). Long-term legacy of massive carbon input to the Earth system: Anthropocene versus Eocene. *Philosophical Transactions of the Royal Society A: Mathematical, Physical and Engineering Sciences*, *371*, 20120006. https://doi.org/10.1098/rsta.2012.0006

Zijderveld, J. D. A. (1967). A.C. demagnetization of rocks: Analysis of results. In D. W. Collinson, K. M. Creer, & S. K. Runcorn (Eds.), *Methods in paleomagnetism* (pp. 254–286). New York: Elsevier.